

# HST/ACS weak lensing analysis of the galaxy cluster RDCS 1252.9–2927 at $z = 1.24^0$

M. Lombardi<sup>1,2</sup>, P. Rosati<sup>1</sup>, J.P. Blakeslee<sup>3</sup>, S. Ettori<sup>1,8</sup>, R. Demarco<sup>3</sup>, H.C. Ford<sup>3</sup>, G.D. Illingworth<sup>5</sup>, M. Clampin<sup>7</sup>, G.F. Hartig<sup>7</sup>, N. Benítez<sup>3</sup>, T.J. Broadhurst<sup>4</sup>, M. Franx<sup>6</sup>, M.J. Jee<sup>3</sup>, M. Postman<sup>7</sup>, R.L. White<sup>7</sup>

[mlombard@eso.org](mailto:mlombard@eso.org)

## ABSTRACT

We present a weak lensing analysis of one of the most distant massive galaxy cluster known, RDCS 1252.9–2927 at  $z = 1.24$ , using deep images from the Advanced Camera for Survey (ACS) on board the Hubble Space Telescope (HST). By taking advantage of the depth and of the angular resolution of the ACS images, we detect for the first time at  $z > 1$  a clear weak lensing signal in both the  $i$  (F775W) and  $z$  (F850LP) filters. We measure a  $5\sigma$  signal in the  $i$  band and a  $3\sigma$  signal in the shallower  $z$  band image. The two radial mass profiles are found to be in very good agreement with each other, and provide a measurement of the total mass of the cluster inside a 1 Mpc radius of  $M(< 1 \text{ Mpc}) = (7.3 \pm 1.3) \times 10^{14} \text{ M}_\odot$  in the current cosmological concordance model  $h = 0.70$ ,  $\Omega_m = 0.3$ ,  $\Omega_\Lambda = 0.7$ , assuming a redshift distribution of background galaxies as inferred from the Hubble Deep Fields surveys. A weak lensing signal is detected out to the boundary of our field (3' radius, corresponding to 1.5 Mpc

---

<sup>1</sup>European Southern Observatory, D-85748 Garching bei München, Germany.

<sup>2</sup>University of Milan, Department of Physics, via Celoria 16, I-20133 Milan, Italy.

<sup>3</sup>Department of Physics and Astronomy, Johns Hopkins University, Charles and 34th Street, Bloomberg Center, Baltimore, MD 21218.

<sup>4</sup>Racah Institute of Physics, Hebrew University, Jerusalem 91904, Israel.

<sup>5</sup>UCO/Lick Observatory, University of California, Santa Cruz, CA 95064.

<sup>6</sup>Leiden Observatory, Postbus 9513, 2300 RA Leiden, Netherlands.

<sup>7</sup>STScI, 3700 San Martin Drive, Baltimore, MD 21218.

<sup>8</sup>INAF, Osservatorio Astronomico di Bologna, via Ranzani 1, I-40127 Bologna, Italy

<sup>0</sup>Based in part on observations obtained at the European Southern Observatory using the ESO Very Large Telescope on Cerro Paranal (ESO program 166.A-0701).

at the cluster redshift). We detect a small offset between the centroid of the weak lensing mass map and the brightest cluster galaxy, and we discuss the possible origin of this discrepancy. The cumulative weak lensing radial mass profile is found to be in good agreement with the X-ray mass estimate based on *Chandra* and *XMM-Newton* observations, at least out to  $R_{500} \simeq 0.5$  Mpc.

*Subject headings:* galaxies: cluster: individual: RDCS 1252.9-2927 – cosmology: gravitational lensing – cosmology: observations – cosmology

## 1. Introduction

Cluster of galaxies lie at the extreme of the mass spectrum of gravitationally bound structures, and therefore their physical properties are thought to be mainly driven by gravitational processes. The study of the mass distribution of galaxy clusters conveys precious information on the relationship between dark and luminous matter and can be used to test cosmological models (e.g. Eke et al. 1996; Bahcall & Fan 1998).

Over the last decade, gravitational lensing has proved to be a powerful method to determine the mass and the mass distribution of galaxy clusters (see Bartelmann & Schneider 2001 for a review). The weak lensing technique, based on a statistical analysis of small distortions of faint background sources, is a particularly valuable tool since it relies on simple, well verified assumptions and is sensitive to the *total* mass of a cluster, regardless of its physical state and spatial distribution.

Following the early work of Tyson, Wenk, & Valdes (1990), many massive clusters have been the subject of weak lensing analyses (e.g. Seitz et al. 1996; Squires et al. 1996; Lombardi et al. 2000). In most cases, these studies focused on many clusters at low-to-medium redshifts ( $0.1 < z < 0.5$ ), for which moderately deep imaging is sufficient to successfully apply this technique. The first attempt to study the weak lensing signal of a high-redshift cluster (Cl 1604+4304 at  $z = 0.89$ ) was not successful (Smail et al. 1994; but see Margoniner et al. 2005 for a recent weak lensing detection). The velocity dispersion of this cluster was initially estimated to be  $1226_{-154}^{+245}$  km s $^{-1}$  (Postman et al. 1998), however a recent extensive spectroscopic study (Gal & Lubin 2004) has found a clear evidence for a superposition of four moderate mass systems (with velocity dispersions  $\sigma_v \lesssim 800$  km s $^{-1}$ ) within  $\Delta z \simeq 0.1$ . Luppino & Kaiser (1997) reported the first clear detection of a weak-lensing signal from a distant cluster, MS 1054.4–0321 at  $z = 0.83$ , using deep ground-based images. An improved analysis of MS1054 was presented by Hoekstra et al. 2000) using HST/WFPC2 observations, which showed the power of weak lensing studies with HST when point spread function

(PSF) effects are properly taken into account. Weak lensing analysis of very luminous X-ray clusters at  $z \simeq 0.8$  is by now relatively straightforward (e.g. Clowe et al. 1998 studied MS 1137.5+6625 at  $z = 0.783$  and RXJ 1716.4+6708 at  $z = 0.809$ ; Huo et al. 2004 studied RXJ 0152.7–1357 at  $z = 0.83$ ).

Weak lensing studies of clusters at  $z \gtrsim 1$  are instead particularly challenging and essentially impossible with ground-based observations. Most of the galaxies observed even in the deepest ground-based observations have redshifts smaller than unity, and thus are foreground with respect to high-redshift clusters, or are only weakly lensed. To avoid a severe dilution of the lensing signal one needs to accurately select background galaxies, typically using photometric redshifts. In addition, galaxies at redshifts larger than unity are faint and small, so that measurements of their ellipticities, needed for the weak lensing analysis, are difficult because of photometric uncertainties and the smearing effect of the PSF (in addition to the seeing in ground-based images). Finally, because of the redshift dependence of the lensing signal, weak lensing masses of distant clusters are strongly sensitive to the redshift distribution of the background galaxies. For example, it is relatively easy to show that a systematic relative error of 5% on  $(1+z)$  of the background galaxies produces a systematic error of 15% on the lensing mass estimate of a  $z = 1$  galaxy cluster.

The advent of the Advanced Camera for Surveys (ACS) on board of the HST has given a unique opportunity to study the mass distribution of clusters at redshift larger than unity via weak lensing techniques. The combination of the excellent PSF and the much improved CCD sensitivity overcomes many of the challenges posed by distant clusters. In this paper, we report an unambiguous weak lensing detection of the galaxy cluster RDCS 1252.9–2927 at redshift  $z = 1.237$  (hereafter RDCS1252 for brevity) using a mosaic of four ACS pointings in the  $i$  and  $z$  bands, the first of this kind at  $z > 1$ .

The paper is organized as follow. In Sect. 2 we describe the observations and data reduction. The weak lensing analysis is presented in Sect. 3 and the results obtained are discussed in Sect. 4. In Sect. 5 we summarize our conclusions. Finally, App. A briefly reports on the mass aperture statistics.

We adopt the current “concordance” cosmological model:  $H_0 = 70 \text{ km s}^{-1} \text{ Mpc}^{-1}$ ,  $\Omega_m = 0.3$ , and  $\Omega_\Lambda = 0.7$ . In this model, one arcminute at the cluster redshift corresponds to a linear size of 0.5 Mpc.

## 2. Observations

RDCS1252 was originally discovered as an extended X-ray source in the *ROSAT* Deep Cluster Survey (RDCS; Rosati et al. 1998) and since then has been the target of a large number of follow-up observations, which include a VLT Large Program with FORS2 optical imaging and spectroscopy and ISAAC deep near infrared imaging (Lidman et al. 2004).

RDCS1252 was observed in the F775W and F850LP bandpasses in May 2002 and June 2002 with the HST/ACS Wide Field Camera as part of the Guaranteed Time Observation program (proposal 9290). The observations were done in a  $2 \times 2$  mosaic pattern, with 3 and 5 orbits of integration in F775W and F850LP, respectively, at each of the four pointings. Two exposures were taken per orbit, and we dithered by 2 pixels in both the  $x$  and  $y$  directions between orbits. However, the imaging was split between two ‘epochs’ separated in time by about six weeks, and there was a  $\sim 20$  pixels ( $1''$ ) offset in the pointing between the two epochs as a result of differences in the guide star acquisition. The first three orbits of F850LP imaging for each position was done during the first epoch (early/mid May), while the remaining two orbits in F850LP and all three orbits in F775W were done during the second epoch (mid/late June).

These data have been described by Blakeslee et al. (2003b), who processed the images as a single large mosaic using *Apsis* (described by Blakeslee et al. 2003a) and studied the color-magnitude relation of cluster galaxies. In order to improve the modeling of the point spread function (PSF) variations, we processed each of the four pointing separately with *Apsis* and used an output scale of  $0.025$  arcsec pixel $^{-1}$  to achieve exquisite PSF sampling. We also used the Gaussian *drizzle* (Fruchter & Hook 2002) interpolation kernel because the resolution-preserving quality of the Lanczos kernel used by Blakeslee et al. (2003b) is not necessary in case of oversampling. We calibrate our photometry to the AB system using zero points of 25.654 and 24.862 for F775W and F850LP, respectively (Sirianni et al. 2004, in preparation) and adopt a Galactic reddening for this field of  $E(i-z) = 0.041$  mag based on the Schlegel et al. (1998) dust maps.

The cluster was also the object of deep observations with *Chandra* and *XMM-Newton* (see Rosati et al. 2004). These data have provided a fairly accurate temperature and metallicity of the intra-cluster gas,  $kT = (6.5 \pm 0.5)$  keV and  $Z = 0.49_{-0.13}^{+0.08} Z_{\odot}$  (if the *Chandra* data alone are used, we obtain  $kT = 6.5_{-0.9}^{+0.5}$  keV and  $Z = (0.60 \pm 0.22) Z_{\odot}$ ).<sup>1</sup> Thanks to

---

<sup>1</sup>The X-ray data analysis in this paper has been here revised with respect to Rosati et al. (2004) and Ettori et al. (2004) by adopting new calibration files (version 2.28), with a proper CTI, time dependent gain corrections, and VFAINT cleaning applied to the event-one file. Moreover, a reverse edge at 2.07 keV is added to the thermal spectrum model as suggested by A. Vikhlinin (private communication) to account for

its high angular resolution, *Chandra* has also revealed some departure from a spherically symmetric distribution of the gas (see below).

### 3. Weak lensing analysis

#### 3.1. Basic relations

In this subsection we briefly review the basic relations used in weak lensing mass reconstructions. We mainly use the notation of Bartelmann & Schneider (2001).

For a gravitational lens at redshift  $z_d$  (in our case  $z_d = 1.237$ ) and a source at redshift  $z > z_d$ , we define the critical density  $\Sigma_c(z)$  as

$$\Sigma_c(z) = \frac{c^2}{4\pi G} \frac{D(z)}{D(z_d)D(z_d, z)}, \quad (1)$$

where  $D(z) = D(0, z)$  and  $D(z_1, z_2)$  is the angular diameter distance between objects at redshift  $z_1$  and redshift  $z_2$ . A lens with projected mass density larger than  $\Sigma_c(z)$  in its core can produce strong lensing effects such as multiple images; instead, a lens with  $\Sigma \ll \Sigma_c(z)$  for any  $z$  only produces weak effects, detectable through a statistical analysis. In the following we will focus on the analysis in the weak lensing regime, while we defer the study of strong lensing effects to another paper.

Accurate measurements of the shapes (ellipticities) of background galaxies lead to the estimate of the lens (reduced) *shear*  $g(\vec{\theta})$  for any angular direction  $\vec{\theta}$ . These shear maps will inevitably have a limited resolution which is basically set by the density of background galaxies (see Lombardi & Bertin 1998). The reduced shear that acts on a given galaxy depends on the galaxy redshift; however, a weak lensing analysis can still be carried out if we know the *redshift distribution*  $p(z)$  of the background galaxies (without knowing necessarily the individual redshifts; see, e.g., Seitz & Schneider 1997). For practical purposes, we can perform the weak lensing analysis *as if* all background galaxies were at the same redshift  $z_{\text{eff}}$  [one can easily show that in the weak lensing limit this is a legitimate simplification; see Eq. (6) below]. In the weak lensing limit, the shear can be directly inverted into the lens *convergence*  $\kappa(\vec{\theta}) = \Sigma(\vec{\theta})/\Sigma_c$  *up to an arbitrary additive constant*; in other words, the transformation  $\kappa \mapsto \kappa' = \kappa + \lambda$  leaves all observables unchanged. This is referred as “mass-sheet degeneracy” and is often broken by fitting the mass profile with a parametric model (and testing to what extent this depends on the model).

---

contamination of the CCD by methylene. As a result, the measured temperature increases by 1–2  $\sigma$  with respect to the results obtained with previous (version 2.21) calibration files.

### 3.2. Ellipticity and shear measurements

The lensing analysis was carried out using the IMCAT software (Kaiser et al. 1995) with some significant modifications (see Luppino & Kaiser 1997; Erben et al. 2001). The whole lensing reduction pipeline, which we describe in detail below, was carefully tested using synthetic field images generated with the *Skymaker* program (Erben et al. 2001).

For each of the four ACS pointings, we combined the  $i$  and  $z$  bands and made a single master catalog. This catalog was used to perform the object detection with the IMCAT hierarchical peak finding algorithm (`hfindpeaks`), using a set of Gaussian kernels with radii in the range  $r_g \in [0.5, 50]$  pixels. The catalog was then visually inspected and spurious detections (such as star spikes, objects close to very bright sources, or near the field edges) were eliminated.

The rest of the analysis was then performed on the  $i$  and  $z$  bands *independently*. We measured the local sky and its gradient around each object by computing the mode of pixel values on 4 annular sectors (with internal/external radii set to 3 and 6 times the detection radius  $r_g$ ) using the IMCAT utility `getsky`. We then performed aperture photometry (`apphot`) and shape measurements (`getshapes`) for each object. Along these steps we explicitly removed closed pairs (i.e. objects whose distance was smaller than  $3r_g$ ) and objects with negative quadrupole moments.

We then classified objects as stars, galaxies, or spurious sources on the magnitude vs. half-light radius  $r_h$  plot. Unsaturated stars occupy a very narrow region on this plot characterized by small  $r_h$ , while well detected galaxies have larger radii; faint objects with sizes comparable to the size of the point spread function were discarded because no clear identification was possible.

For both galaxies and stars we thereby measured the complex ellipticity  $\chi$ . As described in Kaiser et al. (1995) (see also Luppino & Kaiser 1997), the observed ellipticity of an object is related to the true, unlensed ellipticity  $\chi^0$  (in fact, the unlensed ellipticity convolved with an isotropic kernel; see Bartelmann & Schneider 2001 for details) through

$$\chi - \chi^0 = P^g g - P^{sm} q , \quad (2)$$

where  $g$  is the complex shear,  $q$  is a quantity representing the anisotropic part of the PSF,  $P^{sm}$  is the *smear polarizability*, and  $P^g$  is given by

$$P^g = P^{sh} - P^{sm} (P^{sm*})^{-1} P^{sh*} . \quad (3)$$

Here  $P^{sh}$  is the *shear polarizability*, and stars (\*) as superscript denote the corresponding quantities evaluated for stellar objects.

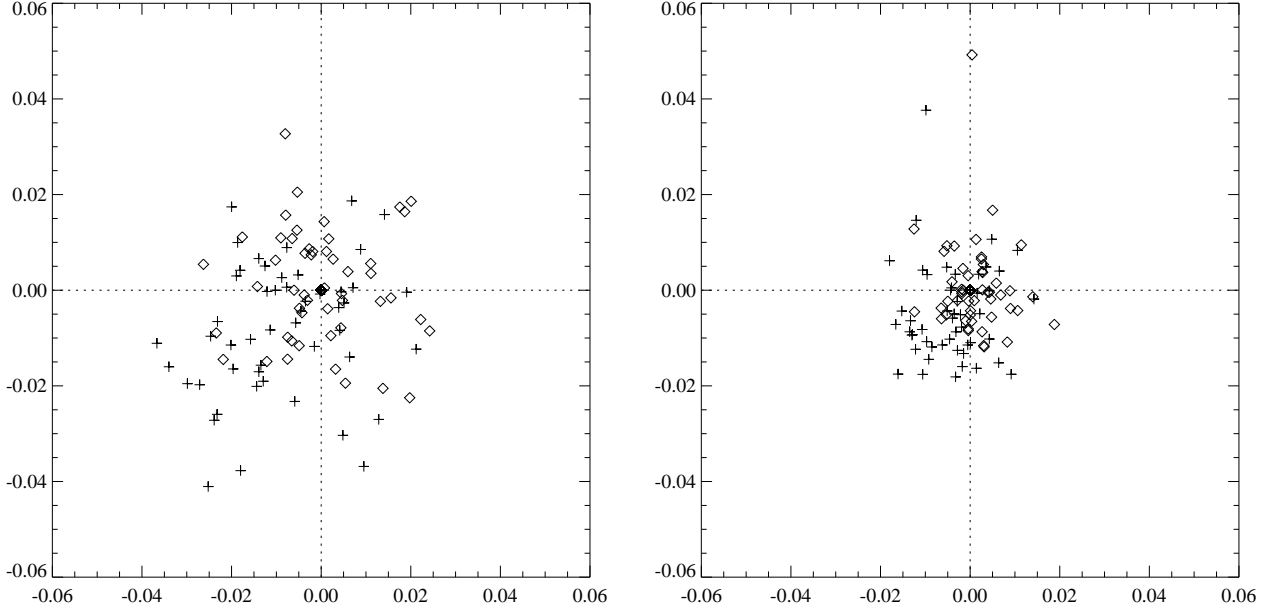


Fig. 1.— The distribution on the complex plane of the star ellipticities  $\chi$  in the  $i$  (left) and  $z$  (right) band. The original, uncorrected ellipticities are marked with crosses, and the corrected ones with diamonds. After the correction, we obtain  $\langle |\chi|^2 \rangle^{1/2} \simeq 0.011$  in  $i$  band and  $\langle |\chi|^2 \rangle^{1/2} \simeq 0.008$  in  $z$  band.

Stars were used to measure the anisotropy of the PSF, characterized by  $q$ , and to calibrate the ellipticity-shear relation, represented by  $P^g$ . Given the relatively low galactic latitude ( $b = +33^\circ$ ) of RDCS1252, more than 300 unsaturated stars are available across the ACS field. Figure 1 shows the observed star ellipticities  $\chi$  in the  $i$  and  $z$  bands on the complex plane. The original, uncorrected star ellipticities were in most cases already very small (RMS below 2%); however, by fitting a second-order polynomial on the field, we obtained star ellipticity residuals as small as  $\langle |\chi|^2 \rangle^{1/2} \simeq 0.011$  for the  $i$  band and  $\langle |\chi|^2 \rangle^{1/2} \simeq 0.008$  for the  $z$  band (this smaller value obtained in the  $z$  band is explained by observing that the size of the isotropic part of the PSF is larger in  $z$  than in  $i$ ). Note that, for each band, the fitting was performed independently on the four ACS pointings. We also verified that the use of individual fits for each of the two ACS chips did not significantly decrease the residuals on the corrected star ellipticities. Figure 2 shows the observed patterns on  $i$  and  $z$  for one of the pointings; the other pointings show consistently similar patterns.

The ellipticity-shear relation was calibrated by measuring the quantity  $(P^{\text{sm}*})^{-1} P^{\text{sh}*}$  for star objects. Following Erben et al. (2001), we evaluated this quantity for each star using different filter scales (with  $r_g$  ranging from 2 to 10 pixels). For any scale, then, we took

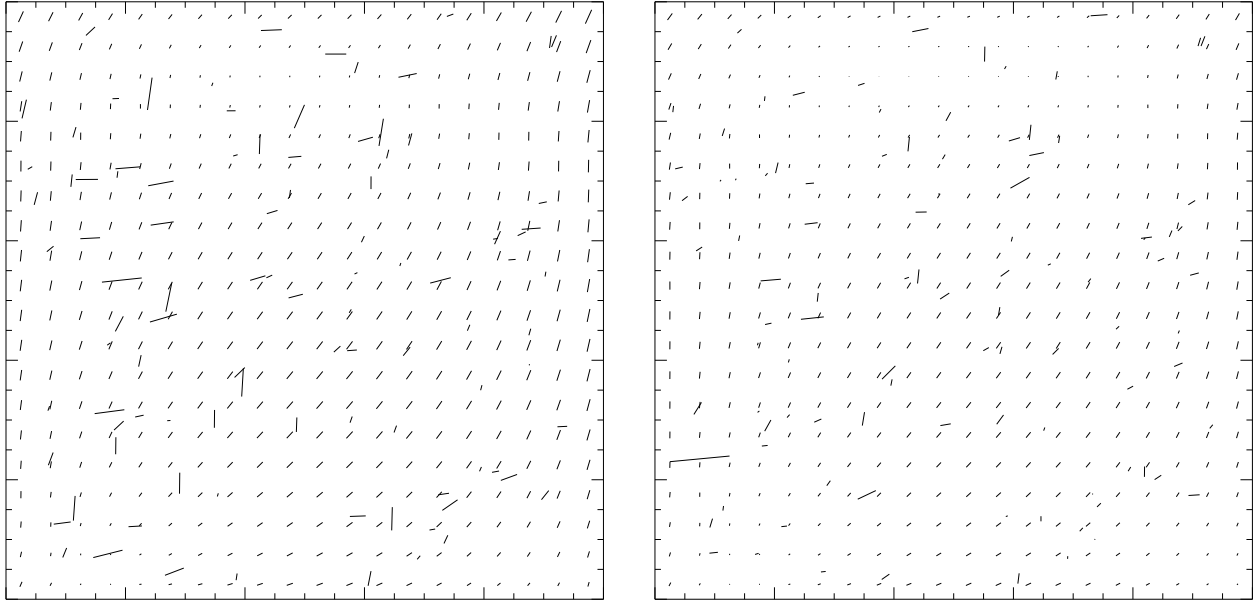


Fig. 2.— The ellipticity pattern in the  $i$  (left) and  $z$  (right) band. We plot the fitted ellipticities (a second order polynomial) on a regular grid ; the original star ellipticities are also marked in this figure at the star locations. The longest tick are associated with ellipticities of  $\sim 3\%$  on the left plot, and  $\sim 5\%$  on the right plot.

the average of this quantity evaluated on all stars. Finally, when calculating  $P^g$  for a given galaxy, we used the scale corresponding to the  $r_g$  of that galaxy.

Since source ellipticities are expected to vanish on average, we obtained an estimate of the complex shear  $g$  acting on each galaxy by taking  $\chi^0 = 0$  and inverting Eq. (2). In order to estimate the error on the shear measurement of each galaxy, we calculated the intrinsic dispersion on the ellipticities for similar galaxies. This was done by calculating the dispersion on the measured shear  $\sum |g|^2/N$  for objects having similar sizes and magnitudes. This dispersion comprises the ellipticity uncertainty due to the photometric error and the intrinsic galaxy ellipticity (the average departure of galaxies from a circular shape), which effectively acts as a source of error for the shear measurements. The photometric error can be conveniently estimated using multiple (two to four) measurements in the overlapping regions by evaluating the differences in the ellipticity of the same galaxy. As an example, in Fig. 3 we show the measured shears of galaxies identified on two adjacent pointings. Interestingly, this plot shows that, for the faint galaxies used in our weak lensing analysis, the photometric error is a significant fraction of the total (photometric and intrinsic) ellipticity error. For example, for the  $i$  band shear estimates we measure an average photometric error  $\text{Err}_{\text{phot}}(g) = 0.148$

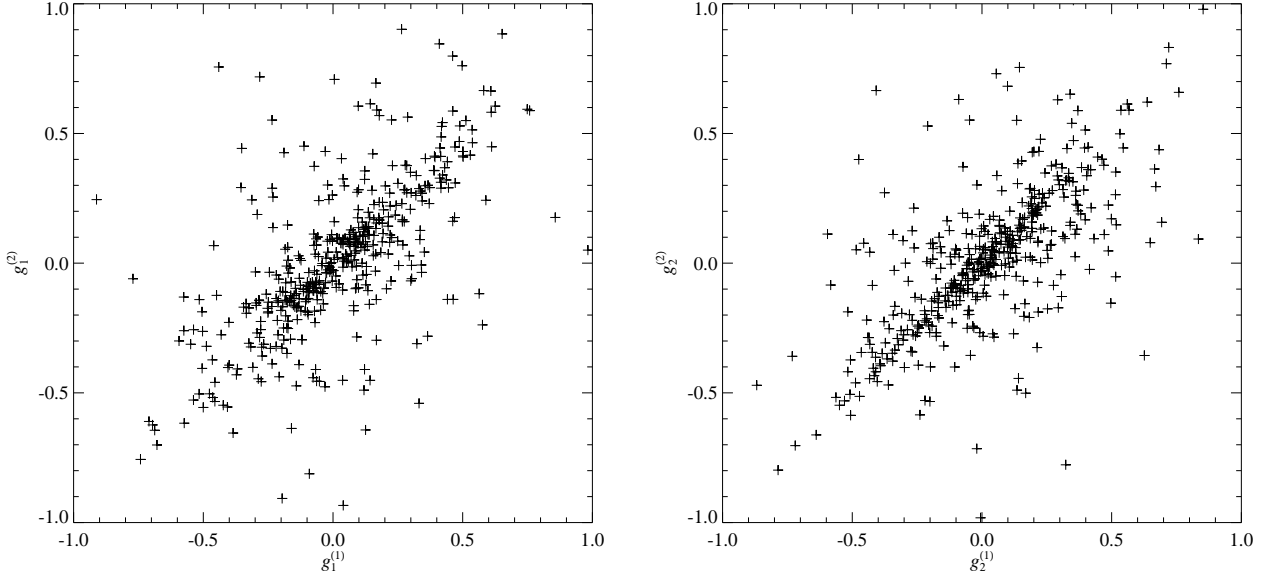


Fig. 3.— Measured galaxy shears of galaxies observed in two adjacent pointings of the  $i$  band mosaic. The left (respectively right) plot shows the real (imaginary) component of the shear measured in the second pointing versus the shear measured in the first one.

and an intrinsic scatter of ellipticity  $\text{Err}_{\text{intr}}(g) = 0.286$  (since the two errors are independent, the total scatter in shear is about  $\langle |g|^2 \rangle^{1/2} = 0.322$ ). Figure 4 shows the photometric errors  $\Delta g$  on the complex plane, and the distribution of photometric errors as a function of the detection significance.

Finally, we merged the four catalogs and replaced multiple entries in the overlapping regions with single ellipticities obtained from a weighted average of the measured shears, and errors evaluated by properly separating the statistical (photometric) and systematic (intrinsic galaxy ellipticity) errors.

### 3.3. Selection of background galaxies

We classified galaxies as background or foreground with respect to the cluster using ground-based photometric redshifts as described in Toft et al. (2004). In particular, we matched the two catalogs obtained from the analysis described above with a catalog containing photometric and spectroscopic redshifts for  $\sim 1200$  objects (see Fig. 5). We then selected as fiducial background objects all galaxies on the photometric redshift catalog with  $z_{\text{phot}} > 1.5$ ; other galaxies too faint to be included in the photometric redshift catalog were taken to be background and included in the final catalog. Finally, we conservatively dis-

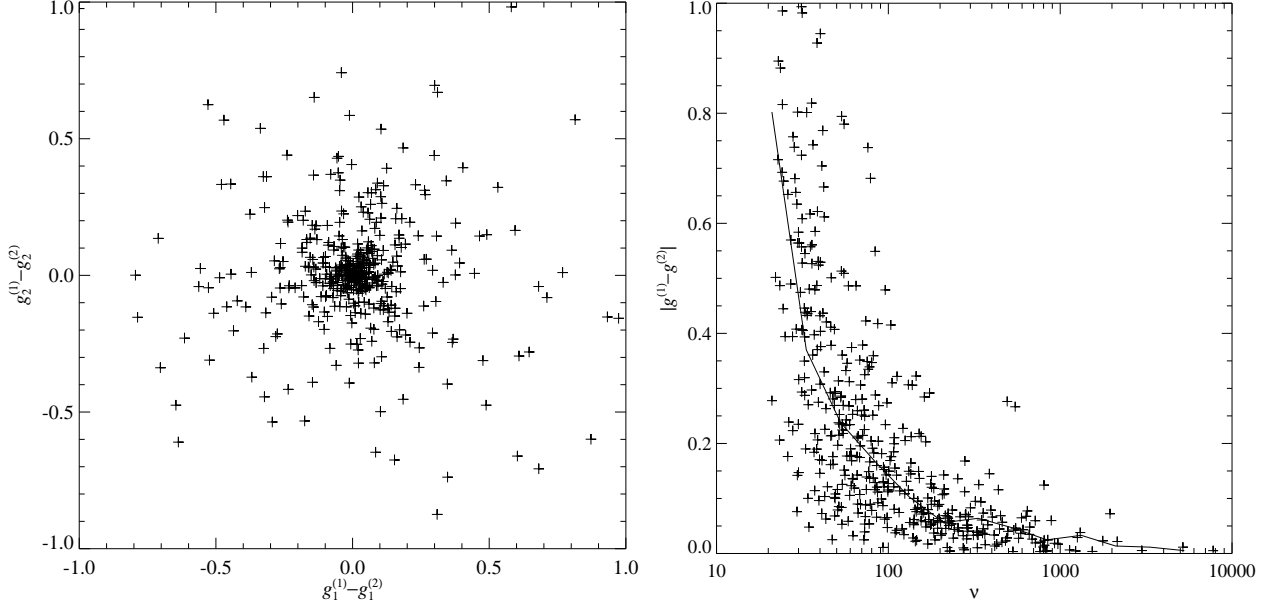


Fig. 4.— Photometric errors on the shear measurements on galaxies observed in two adjacent pointings. Left: differences in the shear real and imaginary parts; note that the errors are isotropic. Right: the error on the shear measurements as a function of the detection significance  $\nu$  of the galaxy. The solid line shows the average error observed for each value of  $\nu$ .

carded for the  $i$ -band (respectively,  $z$ -band) all galaxies with magnitude  $i > 27.4$  ( $z > 26.5$ ) because, in most cases, these objects were too faint to provide reliable shear measurements. These two final catalogs were visually inspected and used for the weak lensing analysis discussed below. The  $i$  band and  $z$  band catalogs contain, respectively, 3 980 and 2 370 galaxies, corresponding to about 120 and 70 galaxies  $\text{arcmin}^{-2}$ . We studied the dependence of the weak lensing signal for different magnitude and photometric redshift cuts, and verified that its strength was maximized for the set of parameters chosen above to select the background galaxy catalog. Interestingly, we were still able to measure a lensing signal when all galaxies were taken to be background and included in the input catalog, although in this case the lensing signal is depressed because of the dilution by foreground galaxies. Figure 5 shows the different galaxy subsamples in a color-magnitude plot, with  $i - z$  derived from ACS isophotal magnitudes.

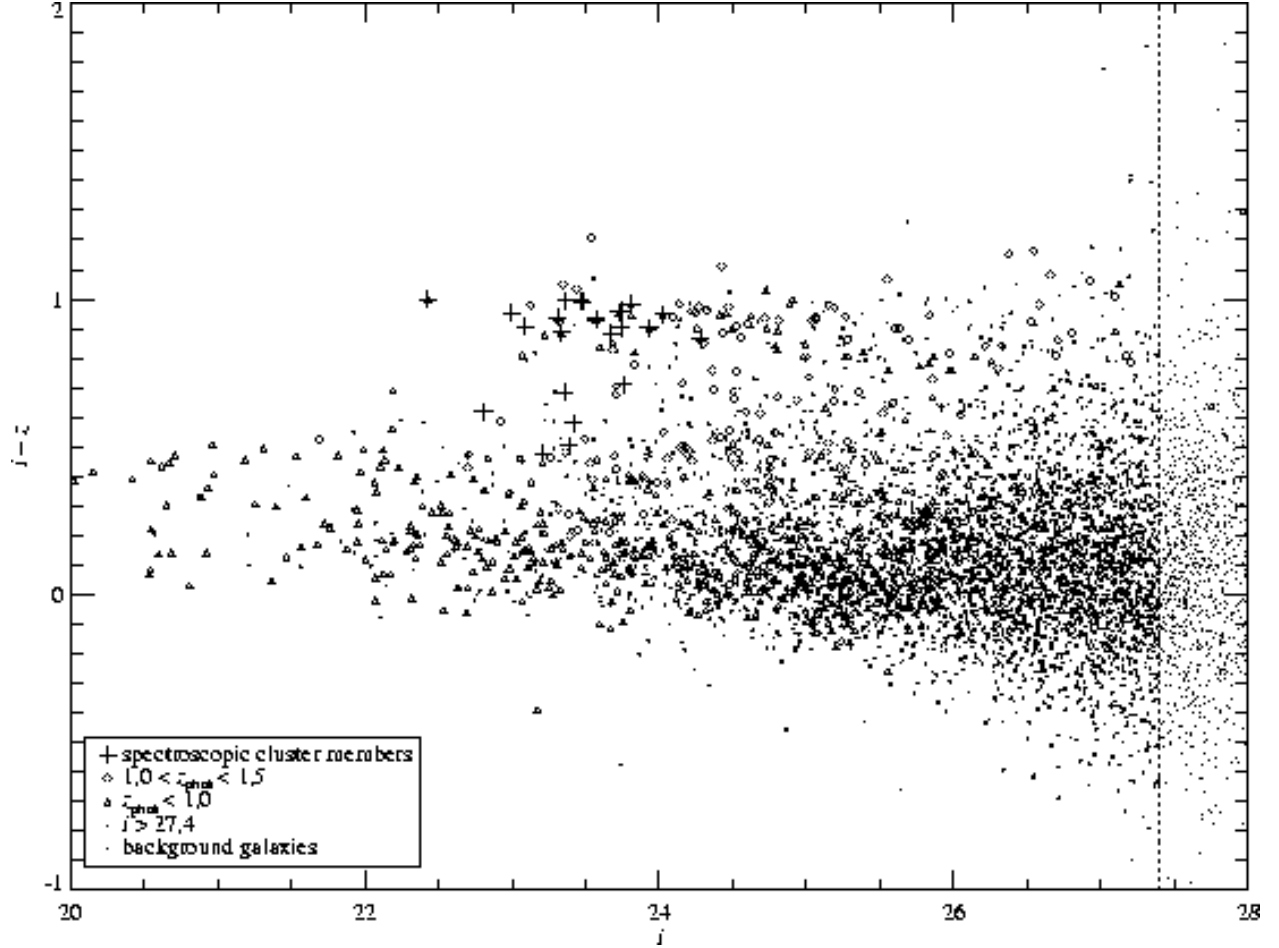


Fig. 5.— The color-magnitude diagram for the galaxies in RDCS1252 field. Objects effectively used for the lensing analysis are marked as “background galaxies.”

## 4. Results

### 4.1. Mass maps

In order to obtain the projected mass distribution of the cluster, we smoothed the galaxy shear estimates into a continuous shear field; the smoothing was performed using a Gaussian kernel characterized by dispersion  $\sigma_W = 25$  arcsec. We inverted the shear field into the convergence using the optimal finite-field inversion algorithm (see Seitz & Schneider 1996; Lombardi & Bertin 1998), with the implementation described by Lombardi & Bertin (1999a). The results are shown in Fig. 6 for both bands.

We also estimated the local error on these maps using two different methods, (i) an

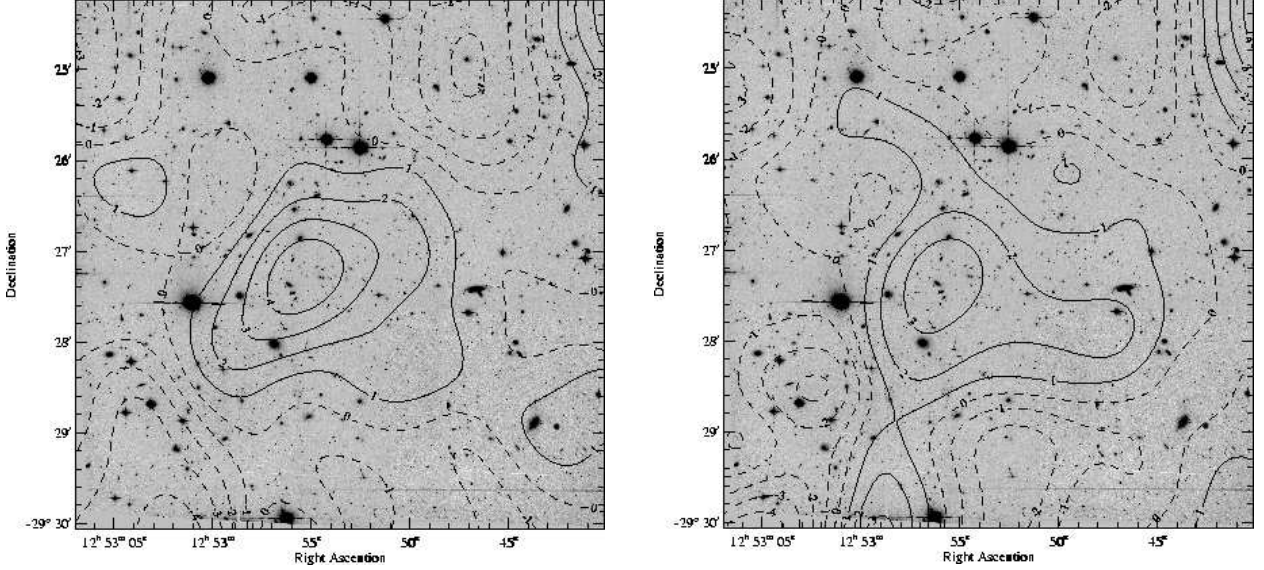


Fig. 6.— Contours of the dimensionless mass maps in the  $i$  (left) and  $z$  (right) bands, overlaid onto the  $i$ -band ACS image. Contours levels are spaced by 0.019 for the  $i$  map and 0.025 for the  $z$  map. These values correspond to the estimated median errors of the two maps over the field (see Fig. 7). Solid (respectively, dashed) contours represent overdensities (underdensities) with respect to the average over the whole field. The mass sheet degeneracy is not removed at this stage, and the mass maps are normalized so that the integrals of them over the whole field vanish.

analytical estimate based on the measured errors on the measured shears for each galaxies (see Lombardi & Bertin 1998) and (ii) a “bootstrap estimate” obtained by assigning galaxy ellipticities drawn from the original catalog to randomly selected galaxy positions (e.g. Efron 1982). These two estimates are in excellent agreement, and give robust statistical significance for the weak lensing detection of RDCS1252 described below. Thus, we could verify that we obtained a  $5\sigma$  lensing signal on the  $i$  band and a  $3\sigma$  detection on the shallower  $z$  band. The predicted analytical errors in the  $i$  and  $z$  maps are shown in Fig. 7 (note that errors are expected to be correlated on the scale  $\sigma_W$  of the Gaussian smoothing applied on the field). As expected, the error is smaller at the center of the field, which is deeper and free from boundary effects. Using these error estimates, we could also optimally combine the  $i$  and  $z$  mass reconstructions into a single field, shown in Fig. 8. The detection significance in this combined map is  $6\sigma$ . We also evaluated the weak lensing mass map using a Gaussian kernel with smaller dispersion,  $\sigma_W = 15$  arcsec. The result, shown in Fig. 9, shows evidence of substructure (note, in particular, the elongation North-South of the main clump, and the presence of several smaller clumps to the West of the cluster core).

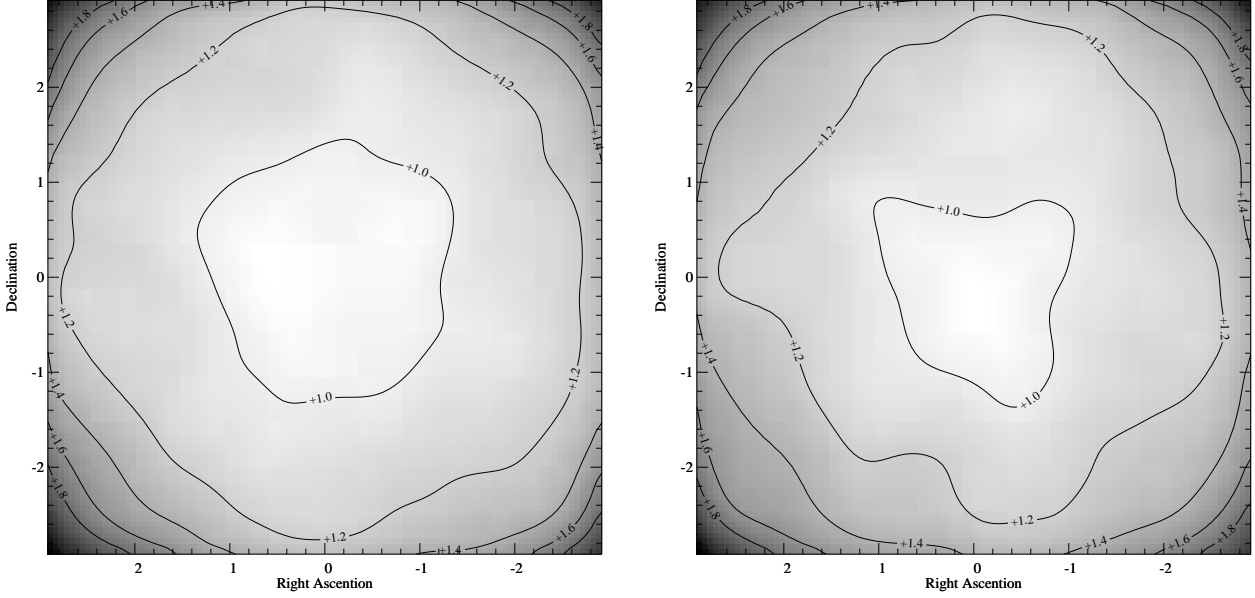


Fig. 7.— The expected local error on the  $i$  (left) and  $z$  (right) mass maps shown in Fig. 6. Contours are labeled in units of median value over the whole field. As expected, the error at the center of the field is below the average, while it increases significantly (by a factor 1.6–1.8) at the corners. The comparison of these maps with the structures observed in Fig. 6 allows us to assess the detection significance of substructures.

In order to check the reliability of our weak lensing detection, we performed several tests. Figure 10 shows an example of a single realization of mass map from a bootstrapped catalog (generated using the  $i$  band catalog); note that the observed convergence is consistent with a vanishing field. A more stringent test for systematic effects was obtained by rotating all galaxy ellipticities by  $45^\circ$ , i.e. by operating the transformation

$$(\chi_1, \chi_2) \mapsto (\chi_2, -\chi_1). \quad (4)$$

and by evaluating the resulting mass distribution  $\kappa_x$ . Because of the properties of the lens mapping, the field  $\kappa_x$  should vanish; moreover, the noise properties of field are very similar to the ones of  $\kappa$ . In this respect we note that, in principle, the noise on the  $\kappa_x$  map is slightly larger, because of the increase on scatter of the lensed ellipticities introduced by the cluster; however, in practice, this effect is expected to be very small for a weak lens such as RDCS1252. The  $\kappa_x$  map is shown in Figs. 11 for the  $i$  and  $z$  bands. Clearly the  $i$  band does not show any significant peak, while the  $z$  band has a few  $2\sigma$  peaks, still consistent with a vanishing field. Given the size of the smoothing performed compared with the size of the field, we have approximately  $10 \times 10$  independent measurements on the whole area; the  $2\sigma$

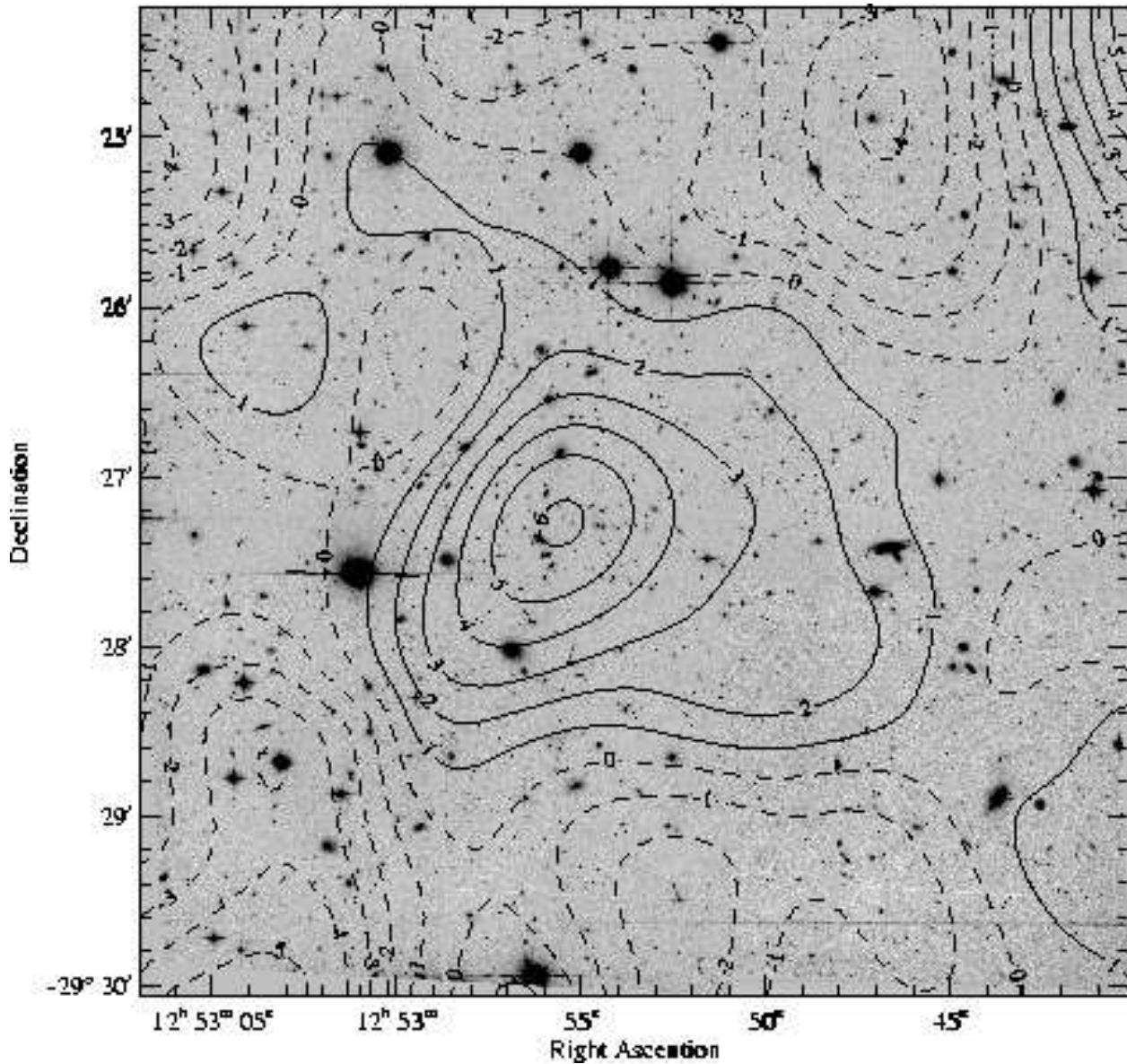


Fig. 8.— The optimally combined mass map of RDCS 1252.9–2927 using both  $i$  and  $z$  ellipticities measurements. Contours are spaced by 0.015, corresponding to the estimated median error of the map over the field.

peaks, in total, occupy about 10% of the field, which is what we would expect from simple statistical arguments.

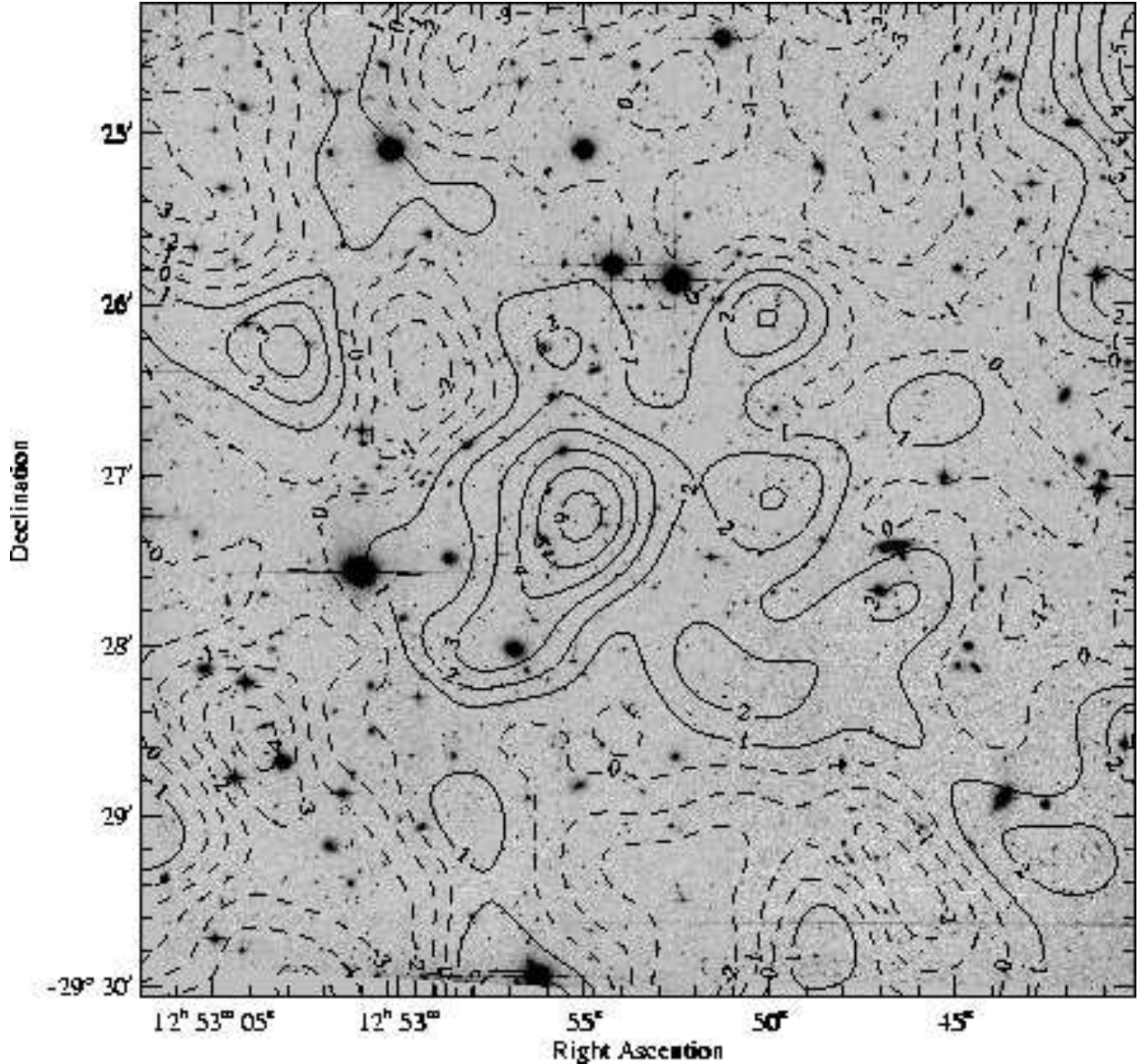


Fig. 9.— Higher resolution mass map of Fig. 8, obtained with a smoothing scale of  $\sigma_W = 15$  arcsec.

To further test the statistical significance of our result, we considered the integral

$$I_x = \int_{\Omega} [\kappa_x(\vec{\theta})]^2 d^2\theta , \quad (5)$$

over the field  $\Omega$  (excluding regions close to the edges of the field in order to avoid boundary effects). The quantity  $I_x$  defined above is clearly always positive, and measures the departure

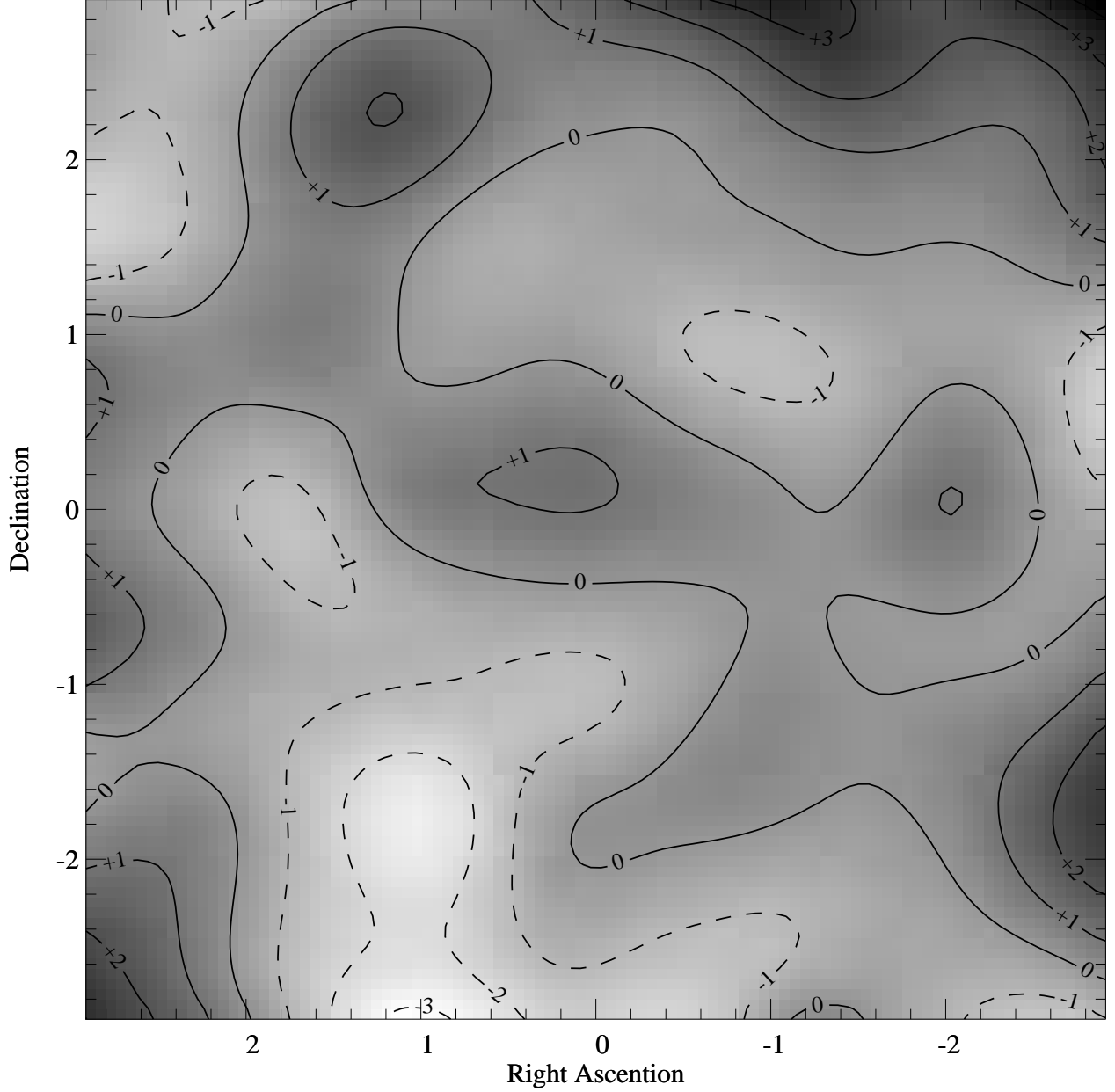


Fig. 10.— An example of realization of a bootstrap shear map in the  $i$  band. Note that the reconstructed mass distribution is consistent with a zero at  $1-\sigma$  level.

of the reconstructed field from a null field. Given its analytical expression, this quantity is expected to behave as a  $\chi^2$ -like distribution. In absence of any systematic effect,  $\kappa_x$  should be consistent with a vanishing field, and thus to have departures from zero consistently with the bootstrapped maps. In other words,  $\kappa_x$  should be statistical indistinguishable from

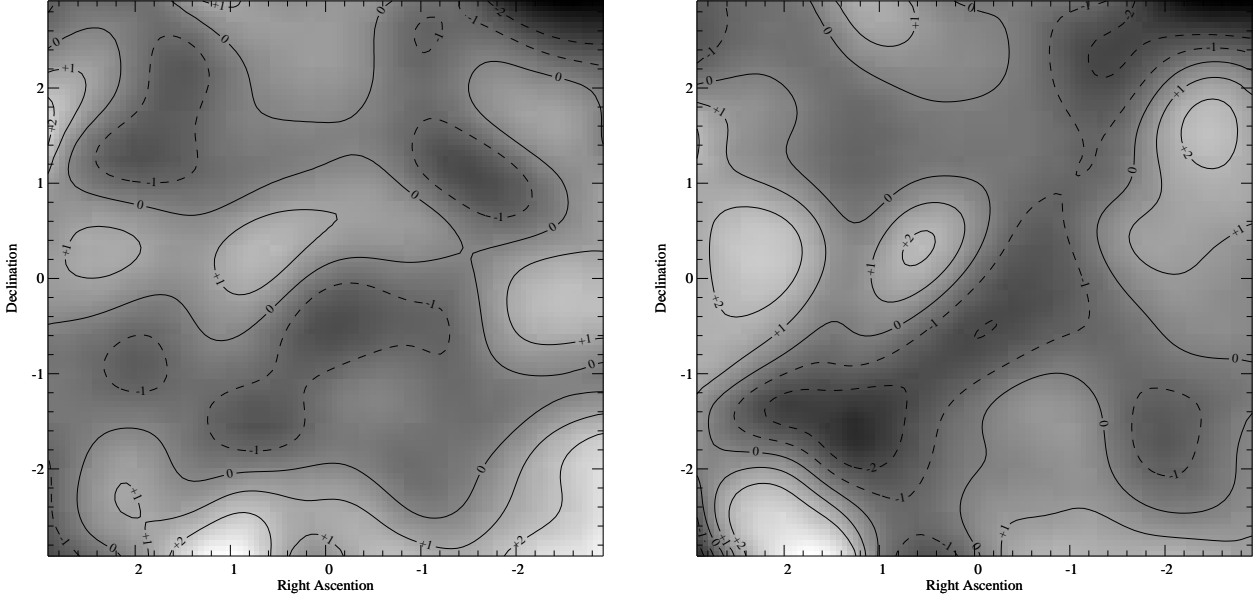


Fig. 11.— The mass distribution obtained by applying the transformation (4) to all galaxy ellipticities in the  $i$  (left) and  $z$  (right) band. Similarly to the other figures, the contours are spaced by  $1-\sigma$ . Since the lensing shear is curl-free, the reconstructed mass map is expected to vanish, which is what we observe (see text).

a bootstrapped map. In order to test this, we compared the value of  $I_x$  obtained from  $\kappa_x$  with the analogous quantity obtained from 1 000 realizations of bootstrapped catalogs. Reassuringly, our analysis shows that in a significant fraction of cases (41% for the  $z$  band and 93% for the  $i$  band) we measured values for  $I_x$  from the bootstrapped maps larger than those obtained from our data. This confirms that both  $i$  and  $z$  band cross convergences are consistent with a zero.

We also evaluated the integral (5) using  $\kappa$  instead of  $\kappa_x$ , and compared the values obtained with the results of the bootstrapping. In the  $i$  band, we had in one single case (out of 1 000) a bootstrapping map with a value exceeding the one observed; in the  $z$  band we had 20 cases out of 1 000; finally, comparing the combined  $i + z$  map and the similar combined bootstrapped maps, we never saw a signal comparable with what we observed.

The overall lensing maps, and in particular Figs. 8 and 9, show a clear elongation of the mass distribution in direction East-West. Although it is generally difficult to evaluate the significance of substructure detections with weak lensing (see, e.g. Marshall et al. 2002), we note *a posteriori* that this elongation is consistent with what inferred from the X-ray and optical contours (see Fig. 12 and discussion in Sect. 4.3). As discussed in Rosati et al. (2004),

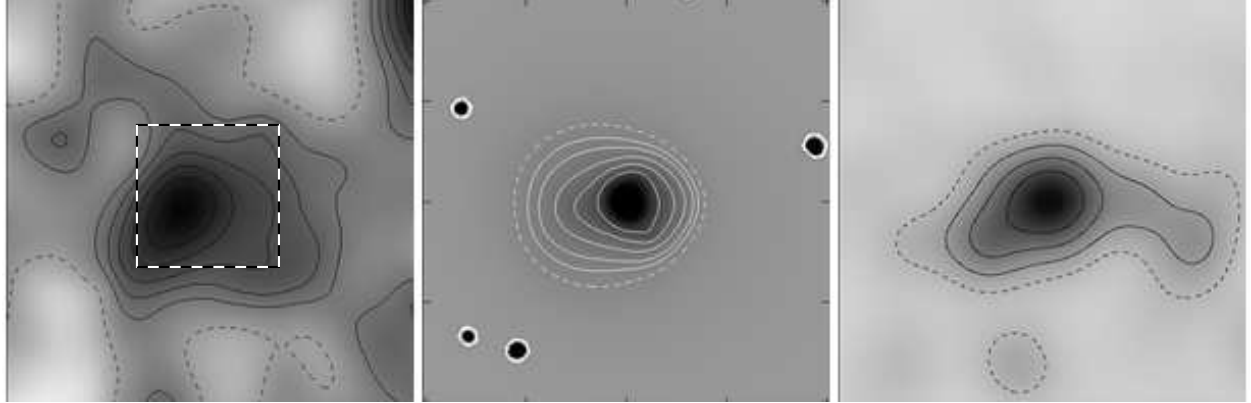


Fig. 12.— From left to right: the weak lensing mass distribution of Fig. 8; the X-ray emitting gas contours, obtained with an adaptive smoothing of the *Chandra* observation in the 1–2 keV; the *K* band luminosity weighted light distribution (Toft et al. 2004). All panels are centered on the optical center of the cluster; the lensing map is  $5.7 \times 5.7$  arcmin $^2$  wide, while the other panels have a side length of 2 arcmin (or 1 Mpc), corresponding to the dashed square in the first panel.

the X-ray surface brightness distribution suggests that we might be observing RDCS1252 in a post-merging phase along the East-West direction. Interestingly, both the shear map and the azimuthally averaged mass map (see Fig. 23 below) extend well beyond the detected X-ray emission, which is affected by severe surface brightness dimming at these redshifts.

In order to convert the dimensionless convergence map into a real mass density field we needed to (i) estimate the redshift distribution of background galaxies and (ii) remove the so-called mass-sheet degeneracy. We will consider these issues in the next two subsections.

#### 4.2. The background redshift distribution

As discussed in Sect. 3.1, the measured (reduced) shear is a function of the redshifts of the background galaxies. Since photometric redshifts are available only for the brightest galaxies (the ones detected on the ground-based images), we estimated the background galaxy redshift distribution  $p(z)$  by resampling the photometric redshift catalogs of the Hubble Deep Fields. We used the catalogs provided by Fernández-Soto et al. (1999) and Lanzetta et al. (2002), and also a newly generated catalog based on the Bayesian photometric redshift estimation (Benítez 2000). Specifically, we matched these catalogs (obtained from HST/WFPC2 observations) with ACS GTO observations in the  $F775W$  and  $F860LP$ .

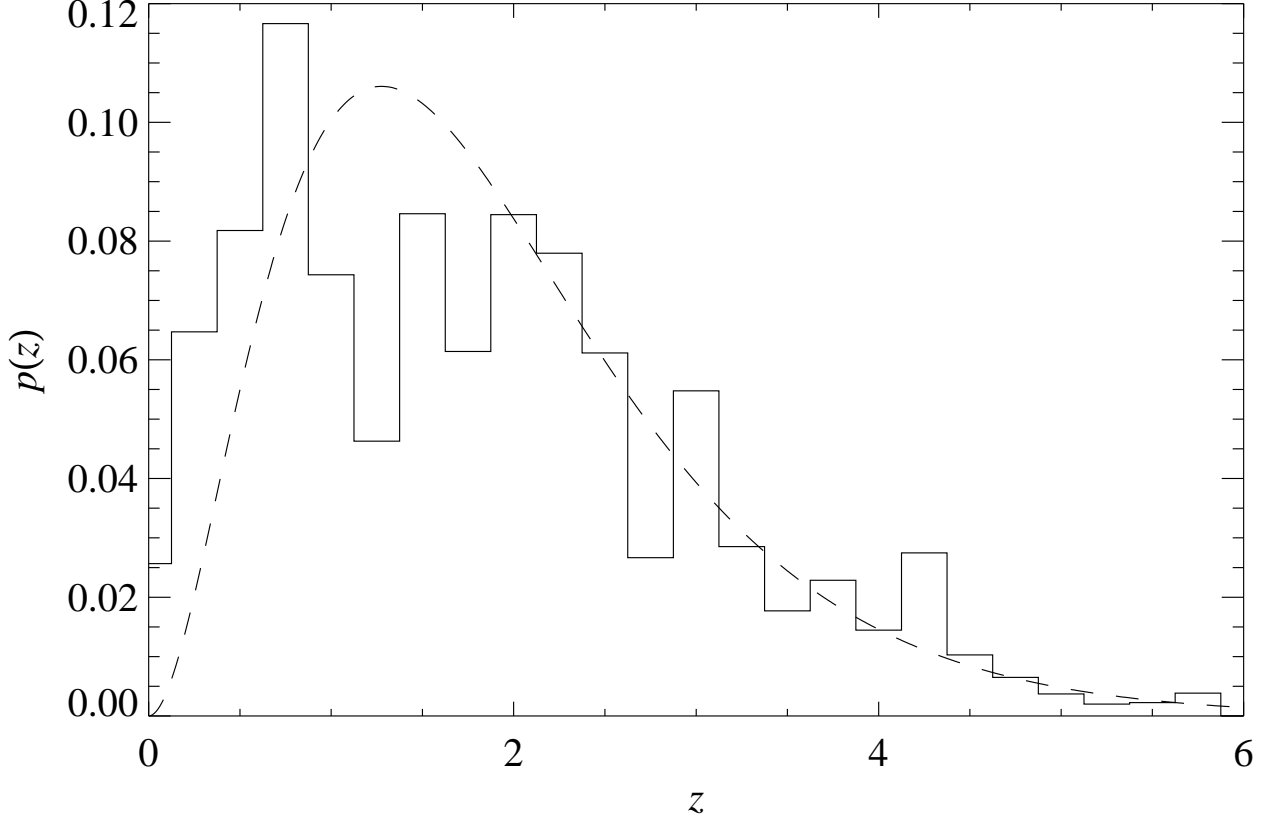


Fig. 13.— The histogram shows the redshift distribution of the galaxy catalog included in the weak lensing analysis, as derived by resampling the Hubble Deep Field North photometric redshift catalog (analyzed using the method by Benitez 2000; see text); the dashed smooth line shows the best fit with simple model for  $p(z)$  of the form (7) with  $z_0 = 1.28$ . Note that the peak of the distribution (mode) is at  $z = z_0$  and the average is  $\langle z \rangle = (3/2)z_0$ .

Thus, we obtained photometry for a sample of approximately 1 000 objects with photometric redshifts in the same filters as RDCS1252 observations. We then divided the HDF catalogs in magnitude bins and derived the  $p(z)$  of galaxies in our field by associating the HDF photometric redshifts in the corresponding bin. Such a method to estimate  $p(z)$  is generally affected by cosmic variance because of the small area covered by the HDFs. We estimate this uncertainty below by comparing the  $p(z)$  derived from the HDF-North and South.

The application of this method to the HDF North led to the redshift distribution shown in Fig. 13 and to an *effective* background source redshift  $z_{\text{eff}}$ . This quantity is defined as the redshift at which all galaxies would need to be in order to produce the same (average)

lensing signal as the galaxies distributed as  $p(z)$ :

$$[\Sigma_c(z_{\text{eff}})]^{-1} = \int p_z(z) [\Sigma_c(z)]^{-1} dz . \quad (6)$$

Using the three HDFs catalogs, we obtained respectively  $z_{\text{eff}} = 1.61$  (HDF-N; Fernández-Soto et al. 1999),  $z_{\text{eff}} = 1.72$  (HDF-N Bayesian estimation; Benítez 2000), and  $z_{\text{eff}} = 1.81$  (HDF-S; Lanzetta et al. 2002). We used  $z_{\text{eff}} = 1.72$  as best estimate, and estimated the error on the effective redshift to be approximately 0.1. We can approximate the galaxy redshift distribution with a simple function of the form (see, e.g. Lombardi & Bertin 1999b)

$$p(z) = \frac{4z^2}{z_0^3} e^{-2z/z_0} , \quad (7)$$

and obtained a best fit value  $z_0 = 1.28$  (see Fig. 13). Although we did not directly use this parametrization in our study, but rather the resampling technique described above, the use of  $p(z)$  in the form of Eq. (7) better elucidates the estimated depth of our observations. Note that  $z_{\text{eff}}$ , which controls directly the scaling between the dimensionless mass distribution  $\kappa(\vec{\theta})$  and the dimensional one  $\Sigma(\vec{\theta})$ , strongly depends on the lens redshift  $z_d = 1.24$ ; the parameter  $z_0$ , instead, only characterizes the background galaxy redshift distribution, and thus can be better used to compare weak lensing studies performed on different clusters. Note that an uncertainty on  $z_{\text{eff}}$  of 0.1 corresponds to a  $\sim 15\%$  uncertainty in final mass estimate.

#### 4.3. Parametric mass estimates

In order to break the mass-sheet degeneracy, which is an intrinsic limitation of parameter-free mass reconstructions, and to better investigate the mass profile, we fitted our data with parametric mass models.

We used both the  $i$  and  $z$  band catalogs, and fitted directly the observed ellipticities with the shear field predicted by parametric mass models. We stress that this allows us to proceed without smoothing, which would be otherwise needed if we were fitting the reconstructed mass distributions (as discussed in Sect. 4.1) or the shear profiles (see below Sect. 4.4). In particular, we used the chi-square function

$$\chi^2 = \sum_{n=1}^N \frac{|g_n - g(\vec{\theta}_n)|^2}{\sigma_n^2} , \quad (8)$$

where  $g_n$  is the measured shear for the  $n$ -th galaxy,  $\sigma_n$  is the associated measurement error (estimated as discussed in Sect. 3.2),  $\vec{\theta}_n$  is the galaxy location on the sky, and  $g(\vec{\theta})$  is the shear predicted by the model chosen (which depends on the model parameters).

Although the mass map shows a slight elongation in direction East-West, we decided to use axisymmetric mass models which are easier to interpret and to compare with independent mass estimates (see below). Thus we used four different models:

**NISwl** A non-singular isothermal sphere centered at the maximum of the weak lensing mass map (R.A.:  $12^h 52^m 55^s.43$ , Dec.:  $-29^\circ 27' 19''.6$ ), which has 2 free parameters (the velocity dispersion  $\sigma_v$  and the core radius  $r_c$ );

**NISf** A non-singular isothermal sphere with free coordinates for its center, which has 4 free parameters ( $\sigma_v$ ,  $r_c$ , and the coordinates of the lens center,  $\vec{\theta}_0$ );

**NFWwl** A NFW profile (see Bartelmann 1996) centered at the maximum of the weak lensing mass map, which has 2 free parameters (the scale radius  $r_s$  and the density  $\Sigma_0 = \rho_s r_s$ );

**NFWf** A NFW profile with free center, which has 4 parameters ( $\Sigma_0$ ,  $r_s$ , and  $\vec{\theta}_0$ ).

The results of the best fit parameters are reported in Table 1 for both the NIS and the NFW models. Note that for both the NIS and the NFW models we obtained mass estimates inconsistent with the virial estimate, based on a measured galaxy velocity dispersion  $\sigma_v \simeq 750 \text{ km s}^{-1}$  (Rosati et al. 2004; see below for a discussion of this point). Results for the NISwl fit performed using *i*-band catalog are shown in Fig. 14, where we plotted the confidence levels obtained from the likelihood ratio technique (see, e.g., Eadie et al. 1971). In order to test the reliability of the likelihood ratio, we generated 1 000 catalogs by adding random errors to the original galaxies ellipticities. In particular, we added to the shear estimates of each galaxy a Gaussian error with variance equal to the estimated shear error. As shown in Fig. 14, the confidence regions reproduce very well the density of fitted parameters (this is

Model	$\vec{\theta}_0$ [arcsec]	$\sigma_v$ [km s $^{-1}$ ]	$r_c$ [arcsec]
NISwl	–	–	1365
NISf	–9.61	+0.10	1185
			5.91
Model	$\vec{\theta}_0$ [arcsec]	$\Sigma_0$ [ $M_\odot \text{pc}^{-2}$ ]	$r_s$ [arcsec]
NFWwl	–	–	320
NFWf	–10.17	1.78	523
			52

Table 1: The best fit parameters for the various models. The center  $\vec{\theta}_0$  is written as celestial coordinates  $\Delta\alpha$  and  $\Delta\delta$  with respect to the peak of the weak lensing map (R.A.:  $12^h 52^m 55^s.43$ , Decl.:  $-29^\circ 27' 19''.6$ ). Note that the scale radius  $r_s$  appearing in the NFW models is intrinsically different from the core radius  $r_c$  of the NIS models.

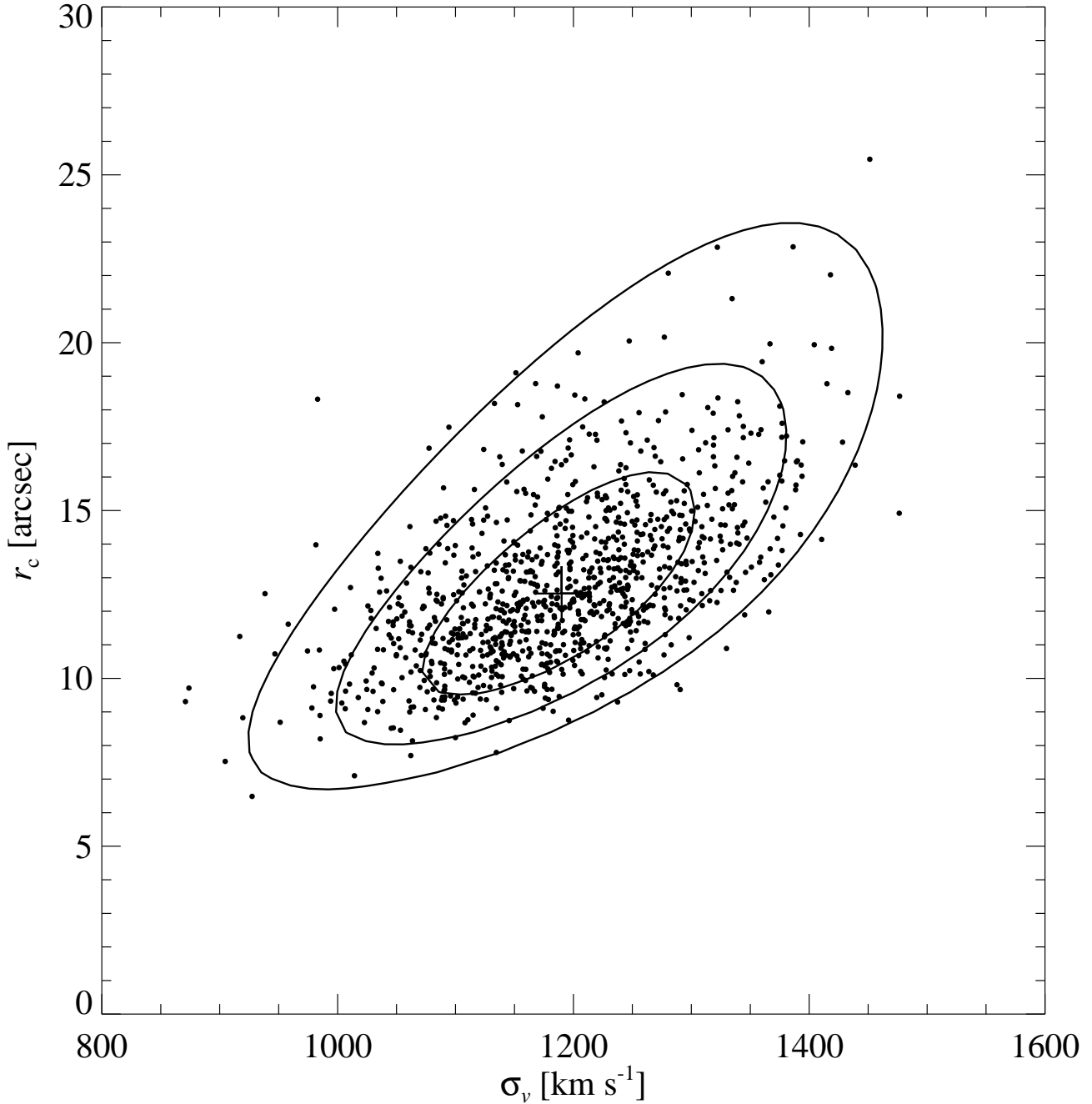


Fig. 14.— Confidence levels for the non-singular isothermal sphere fits NISwl performed on the  $i$  band. The plot shows the 68.2%, 95.4%, and 99.7% confidence regions for the lens velocity dispersion  $\sigma_v$  and core radius  $r_c$ . The points show the best fit parameters obtained by bootstrapping 1 000 catalogs (see text).

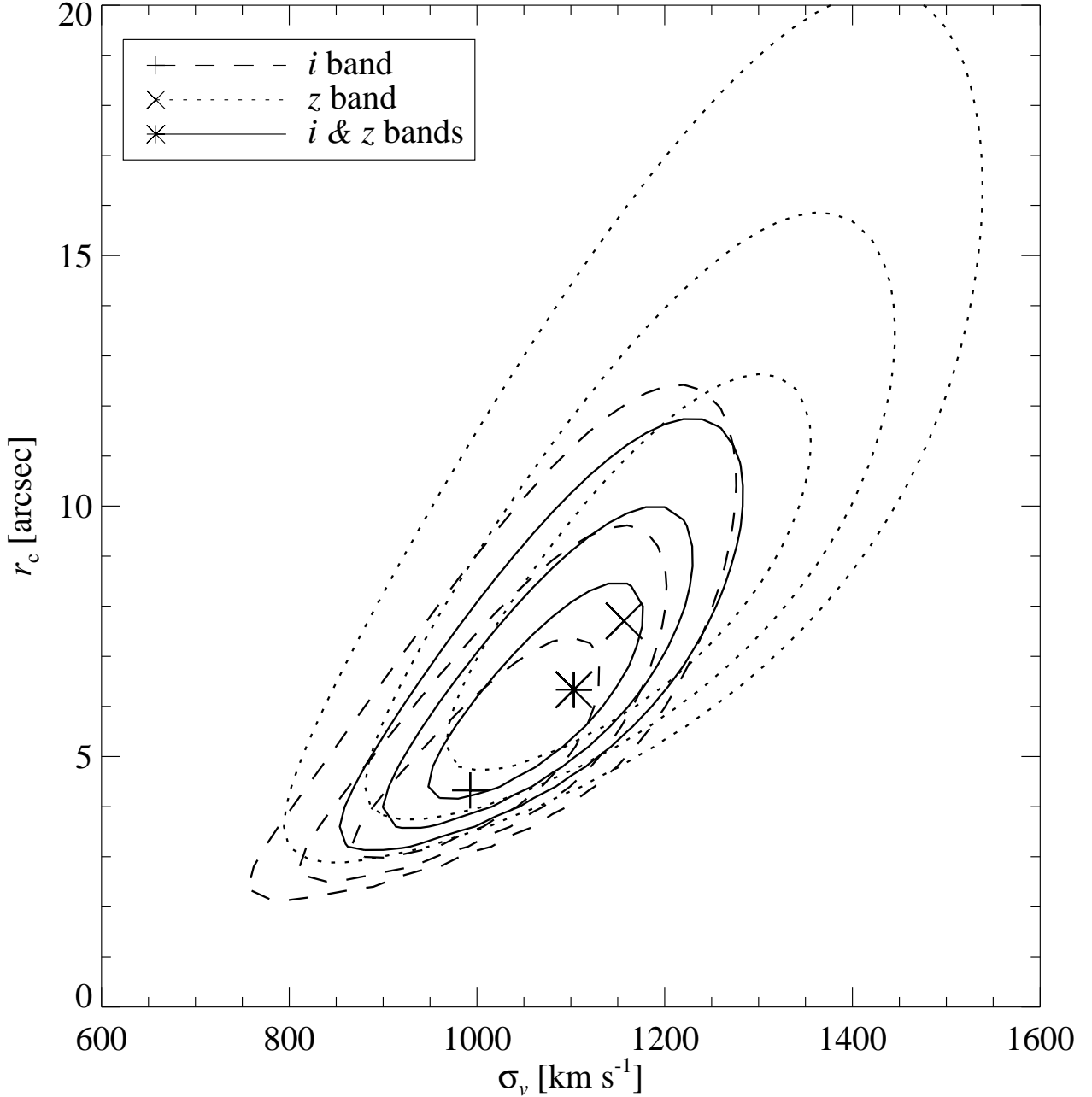


Fig. 15.— Confidence levels for the non-singular isothermal sphere fits NISf. The plot shows the 68.2%, 95.4%, and 99.7% confidence regions for the lens velocity dispersion  $\sigma_v$  and core radius  $r_c$  for the fits performed using the *i* catalog, the *z* catalog, and both. The contours are obtained by marginalizing the results over the lens center (see also Fig. 16). The best fit values are also marked.

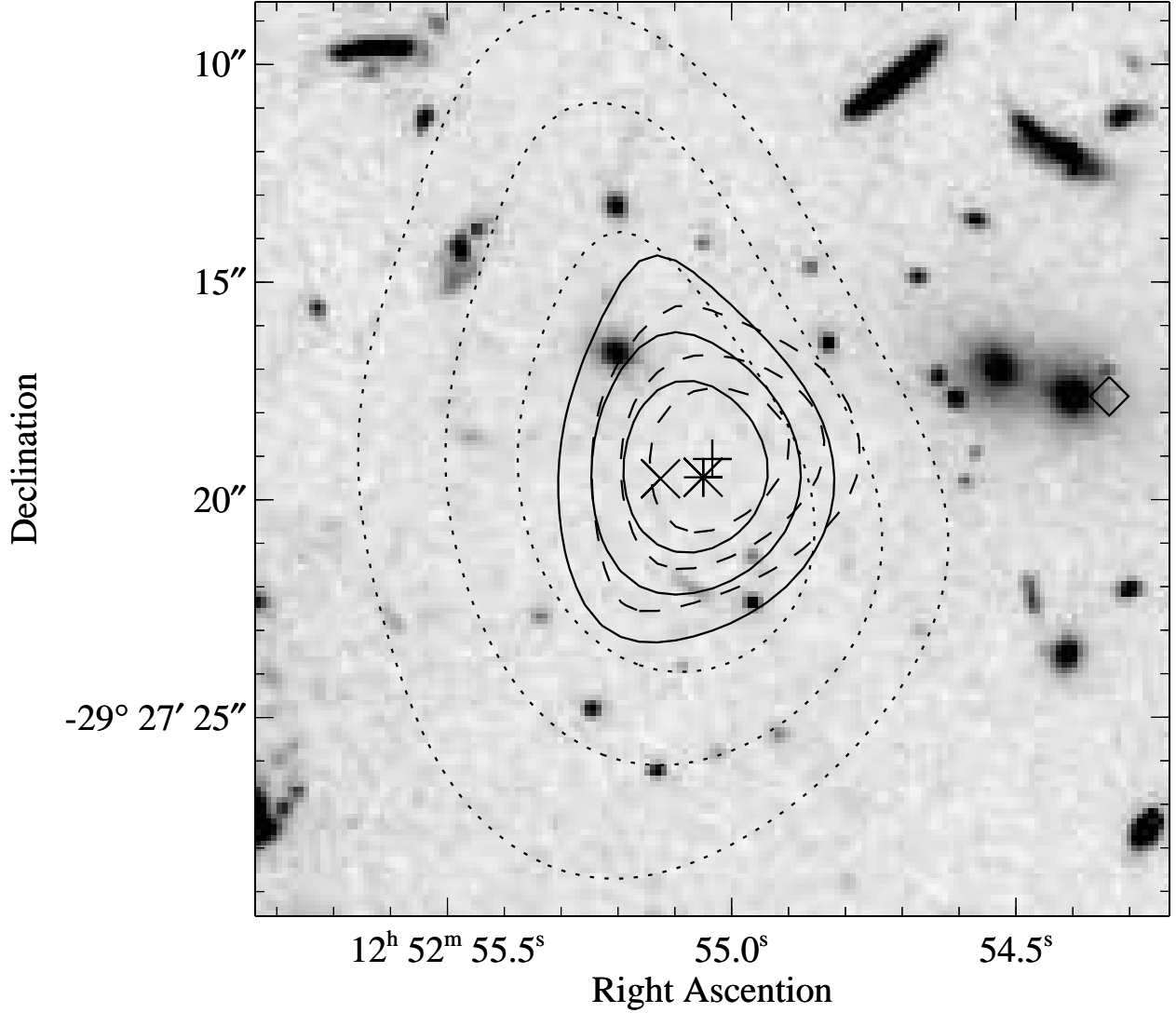


Fig. 16.— Confidence regions corresponding to the other two parameters of the NISf fit, namely the two coordinates of the center of the lens, overlaid onto *i*-band image of the field. The best fit center appears to have a significant offset with respect to the two cD galaxies (center right). Symbols are as in Fig. 15; the centroid of the X-ray emission is marked with a diamond. A similar offset is observed for the NFWf fit.

also confirmed by a quantitative statistical analysis, not reported here). Note that, since the confidence regions shown in Fig. 14 are in a two-dimensional parameter space, the probability of having a velocity dispersion smaller than, say,  $900 \text{ km s}^{-1}$  *regardless* of the value of the core radius  $r_c$  is extremely low (about 1.4%).

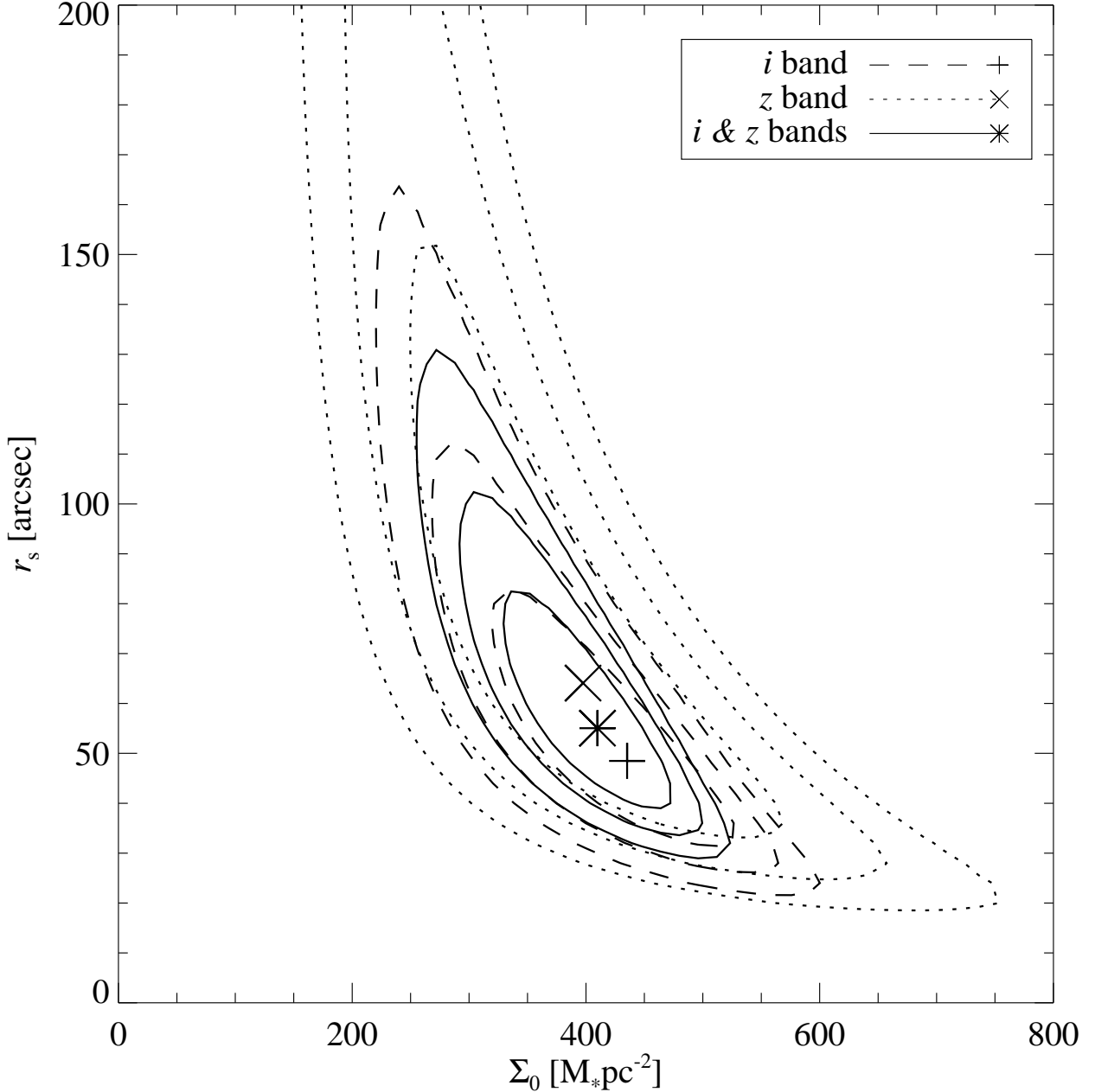


Fig. 17.— Confidence levels for the NFW spherical fit. The plot shows the 68.2%, 95.4%, and 99.7% confidence regions for the lens central density  $\Sigma_0$  and scale radius  $r_s$  for the fits performed using the  $i$  catalog, the  $z$  catalog, and both.

Figure 15 shows confidence regions in the  $\sigma_v - r_c$  slice of the parameter space for the NISf fit; the three regions correspond to the fit performed on the  $i$ ,  $z$ , and  $i + z$  catalogs.

A comparison of the confidence regions for the  $i$  and  $z$  bands shows that the latter have a slight offset toward larger velocity dispersions.

The other slice of the parameter space for the NISf fit, namely the lens position  $\vec{\theta}_0$ , is shown in Fig. 16, together with the  $i$  band image in the background. We observe a significant offset (about 8 arcsec to the East, corresponding to 65 kpc at the redshift of the cluster) of the lens center with respect to the light, and in particular to the two cD galaxies. Interesting, a similar offset is observed also when fitting with the NFWf profile and on the parameter-free mass maps (cf. Figs. 6 and 8). All these observations seem to indicate a real offset between the cluster baryonic and dark matter distributions. Special care is required to interpret this result because (i) the center of the parametrized models could be biased because of the use of simple, radially symmetric profiles; (ii) the offset on the parameter-free maps is much smaller than the smoothing length used to build them ( $\sigma_W = 25$  arcsec); (iii) the center of the weak lensing mass could be offset because of the effect of other intervening mass concentrations (see below Sect. 4.3.3).

A similar analysis was performed for the NFW models. As an example, we report here the confidence regions for the  $\Sigma_0 - r_s$  slice on the NFWf fit are shown in Fig. 17 for the various catalogs.

Finally, we show the mass integral radial profiles for the different fits in Fig. 18; errors for the NIS fit are plotted as vertical segments (errors on the other fits have a similar trend and are not shown here). As pointed out in several studies (e.g. King et al. 2002), weak lensing techniques are not very effective in discriminating among different mass models.

We show in Fig. 18 the X-ray mass measurement, projected along the line of sight, with its uncertainty (see Rosati et al. 2004 for details). We note that the X-ray and lensing mass estimates are consistent within 1 arcmin, which is the radius out to which the X-ray emission can be traced. In particular, the two profiles are statistically indistinguishable up to  $\sim 30''$ – $40''$ ; at larger radii, there is a hint for the weak lensing mass to be slightly larger than the X-ray mass. In general, given the difficulties of both mass measurements, the results obtained are extremely encouraging and provide further evidence that X-ray and weak lensing mass estimates can be in very good agreement to each other when high-quality data are used.

Although the X-ray derived mass compares favorably with the weak lensing analysis, we find useful to describe in the following paragraphs some sources of errors and biases of both methods. The discussion below, though not exhaustive, can be of interests for other weak lensing analyses of high-redshift clusters.

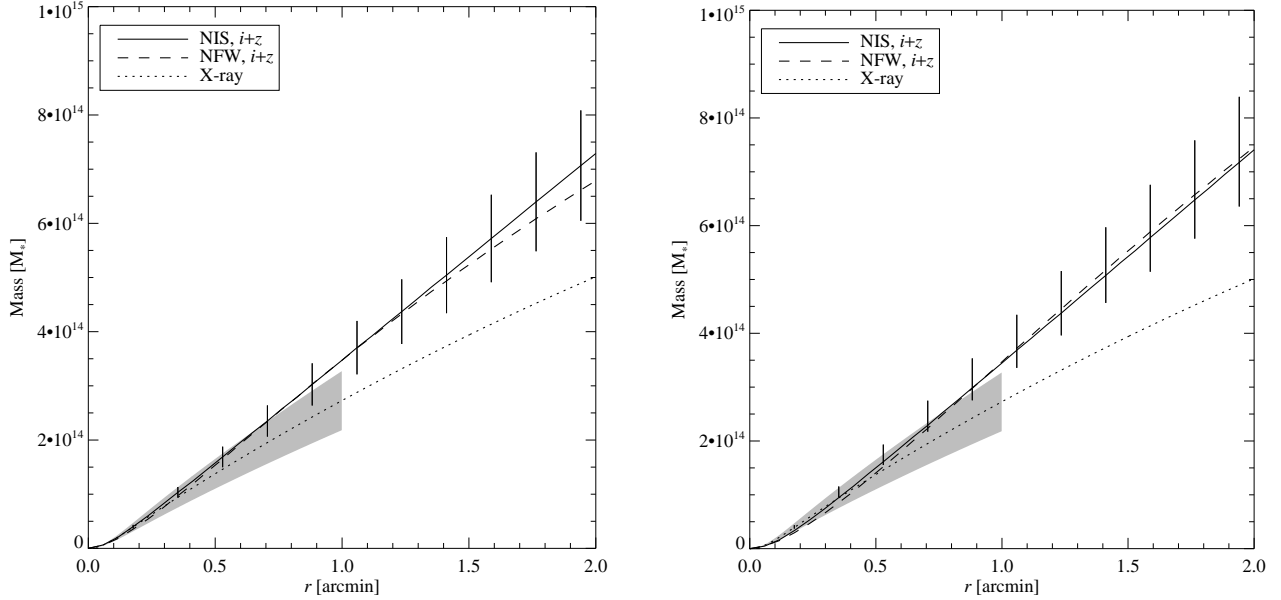


Fig. 18.— The cumulative radial profiles of the best fit NIS and NFW models compared with the projected mass determined from the X-ray data for different temperatures. The gray area denotes the region over which X-ray emitting gas is detected ( $1 \text{ arcmin} \simeq R_{500}$ ), and its thickness represent the estimated  $1-\sigma$  error. Weak lensing mass profiles are derived using the best-fit centers in the left panel, and the X-ray center in the right panel.

#### 4.3.1. Uncertainties on the X-ray mass estimates

The central panel of fig. 12 shows that the surface brightness profile is smooth on the East side, whereas it shows a discontinuity (possibly a cold front) on the West side, where presumably a departure from hydrostatic equilibrium occurs. In order to evaluate the impact of this anisotropy, we recalculated the  $\beta$  model (Cavaliere & Fusco-Femiano 1978, 1976) of the cluster for two sectors located to the East and to the West of the X-ray centroid (see Fig. 5 of Rosati et al. 2004). The results obtained show that there is only a small ( 6%) increase in the mass estimate inside 500–530 kpc if the X-ray  $\beta$  model is derived from the West sector only.

Another source of uncertainty on the X-ray mass estimate is given by the temperature profile. Our X-ray mass estimate assumes an isothermal ICM with a temperature  $T = (6.5 \pm 0.5)$  keV (the best fit from the *Chandra* and *XMM-Newton* data). We investigated the presence of a temperature profile within 60 arcsec from the X-ray center by using the *Chandra* data. By fixing the metallicity at  $0.4 \times Z_{\odot}$ , we measure  $kT = 7.4_{-1.5}^{+2.1}, 6.1_{-1.1}^{+1.4}, 5.5_{-1.9}^{+3.9}$  keV in the radial bins (0–10) arcsec, (10–35) arcsec and (35–60) arcsec, respectively, with

$\sim 300$  net counts each. These values suggest indeed that the gas temperature is higher in the central 35 arcsec than actually assumed for our mass estimate and decreases outward. A polytropic profile with index  $\gamma = \log T / \log n_{\text{gas}} \approx 1.14$  and a central temperature value  $T_0 = (7.6 \pm 2.0)$  keV provides a good fit to the observed temperature profile. Being the mass measurement directly proportional to  $\gamma T_0$  ( $\gamma = 1$  and  $T_0 = T$  for the isothermal case), a direct implication of this negative gradient is that the mass estimates within 60 arcsec are systematically higher than the ones obtained under the isothermal assumption, with values larger by 20% within 20 arcsec. On the other hand, the two estimates agree within 10% at  $R_{500} \simeq 530$  kpc. We note however that the systematic effect introduced by a temperature profile in the X-ray mass measurement is comparable to its statistical uncertainty,  $\sim 35\%$  (1- $\sigma$  level).

#### 4.3.2. Uncertainties on the weak lensing mass

As described above, for such a distant cluster the lensing mass estimate is *strongly* dependent on the assumed redshift distribution of background galaxies, which in this paper has been parametrized using the effective redshift  $z_{\text{eff}}$ . As discussed above, this effect alone introduces an error of  $\sim 15\%$  in our case.

A possible source of systematic error could be ascribed to an inaccurate PSF correction performed by `Imcat`. Although this software has been successfully applied to many ground-based and HST observations, it has never been tested on ACS data, and to our knowledge the weak lensing analysis presented in this paper is the first one carried out with `Imcat` on ACS images. This point will be further investigated on a follow-up paper.

Departure from spherical symmetry and substructures are also a potential source of biases (e.g. Clowe et al. 2004). Although RDCS1252 appear to be fairly round in both X-ray and optical images, the presence of a cold front feature does not exclude substructures in its mass distribution; therefore, the formal errors of the various fit parameters should be taken with caution. This might also contribute to the observed offset between the X-ray/optical and the lensing mass centroids.

#### 4.3.3. Effect of aligned mass concentrations

As pointed out by many authors (e.g. Metzler et al. 2001; White et al. 2002), intervening structures observed along the line of sight of a cluster can have significant effects on its weak lensing mass estimate. For massive clusters at low-to-moderate redshift this effect is typically

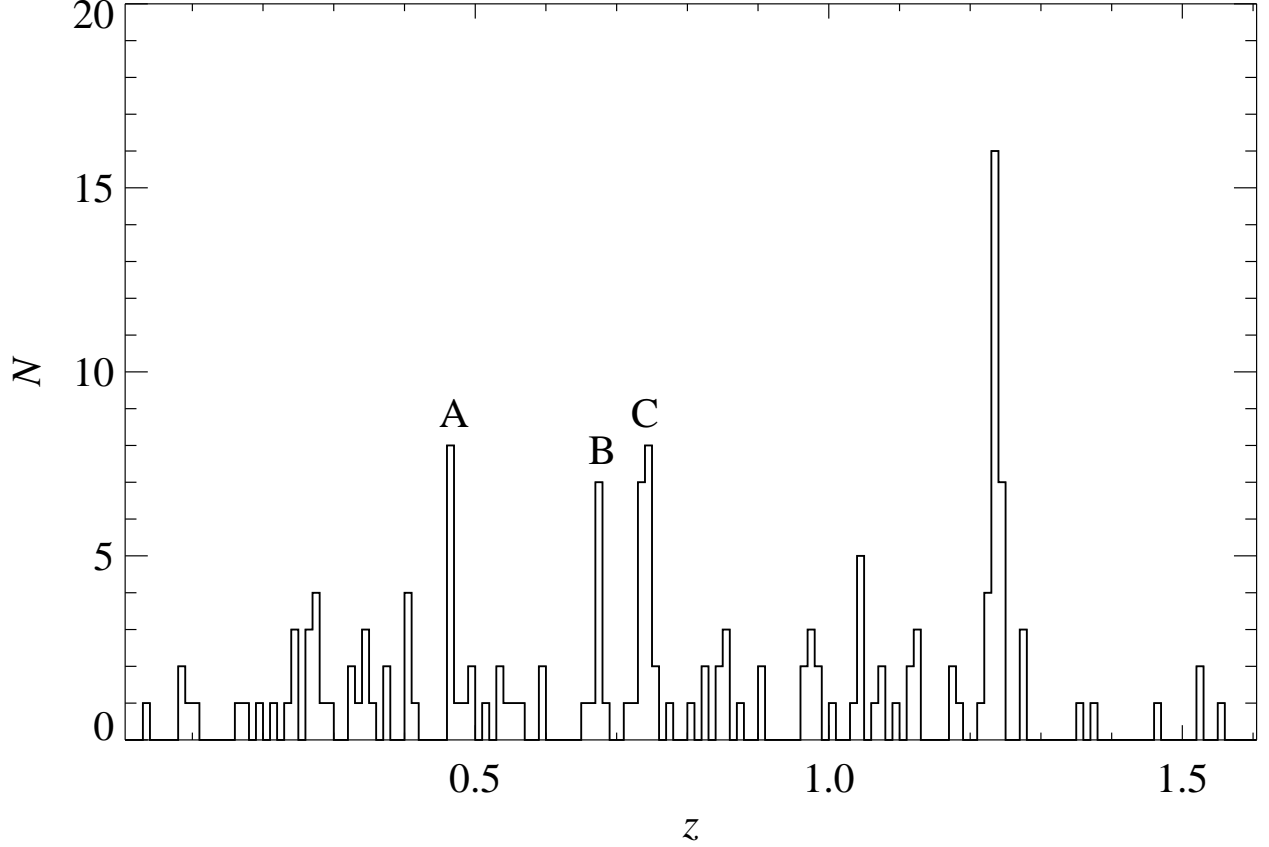


Fig. 19.— Histogram of the measured spectroscopic redshifts in the RDCS1252 field. Three significant foreground groups are marked.

negligible, since it is unlikely that a structure along the line of sight be able to significantly perturb the shear field of the cluster. However, the situation can be quite different if the cluster is not very massive or is either at high or at very low redshift (compared to the average redshift of the background galaxies). In these cases, the weak shear field produced by the cluster can be significantly affected by intervening groups or large scale structures that happen to be aligned along the line of sight.

In order to further investigate this point, we have plotted in Fig. 19 the distribution of the measured spectroscopic redshift on the same field. This figure shows three significant peaks on the distribution around the redshifts 0.47, 0.68, and 0.74 (a closer inspection shows that the  $z \sim 0.74$  peak in the redshift histogram is composed of two peaks separated by  $\Delta z \simeq 0.01$ ). In Fig. 20 we show the angular distribution of the galaxies with measured redshift associated with the various peaks, which appear to correspond to galaxy groups projected along the line of sight of RDCS1252.

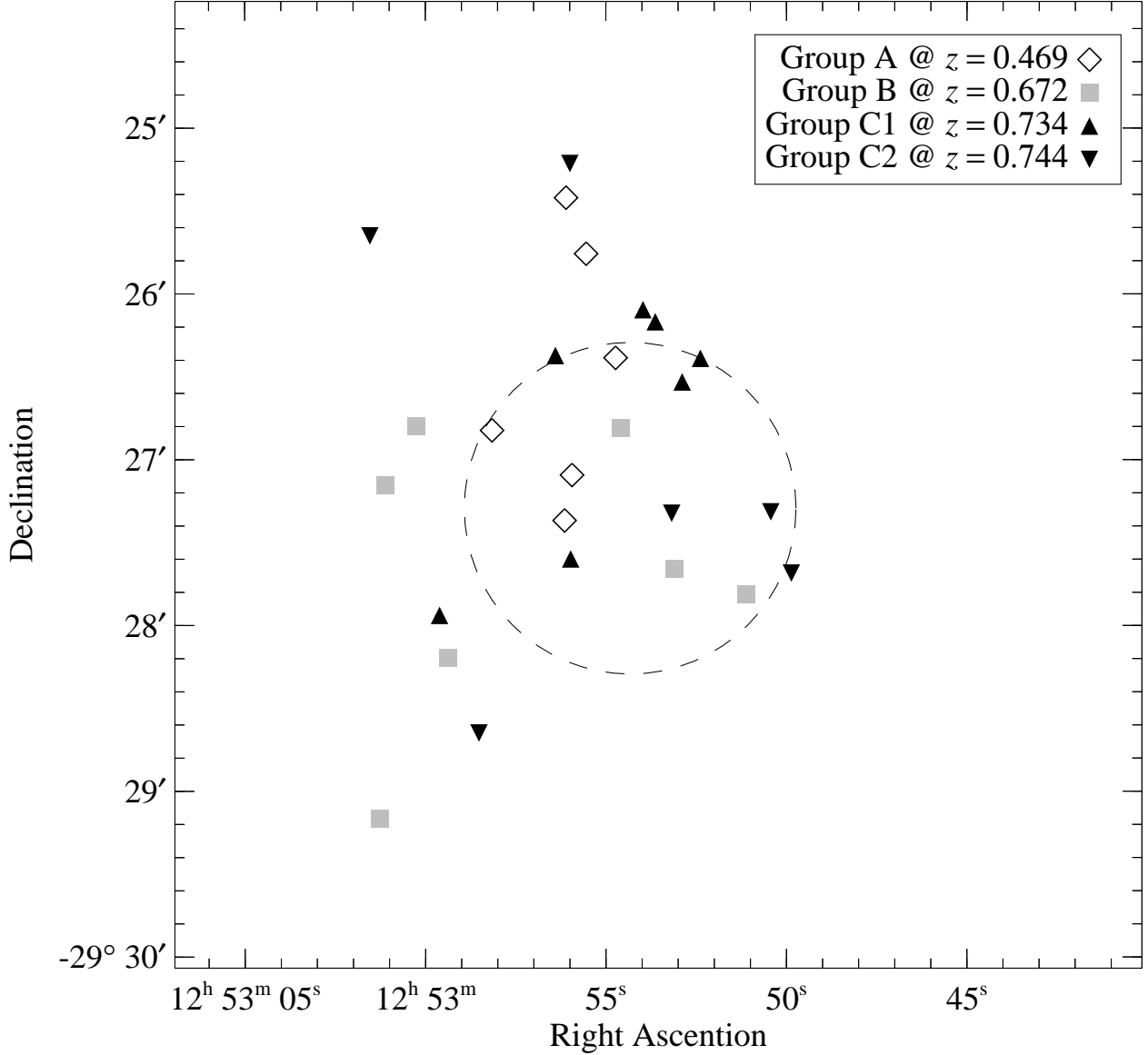


Fig. 20.— The angular distribution of the galaxies belonging to the three redshift peaks identified in Fig. 19. The dashed circle denotes the cluster X-ray/optical center with 1 Mpc diameter.

Because of their lower redshift, these groups can have a non-negligible impact on our weak lensing mass. A quantitative estimate of this effect would require knowledge of individual masses of the various groups, and is thus difficult at this stage. Specifically, a mass of  $5 \times 10^{12} M_{\odot}$  for each group would be responsible for  $\sim 15\%$  of the lensing signal. We also note (cf. Fig. 16) that the contribution from these foreground groups could explain the

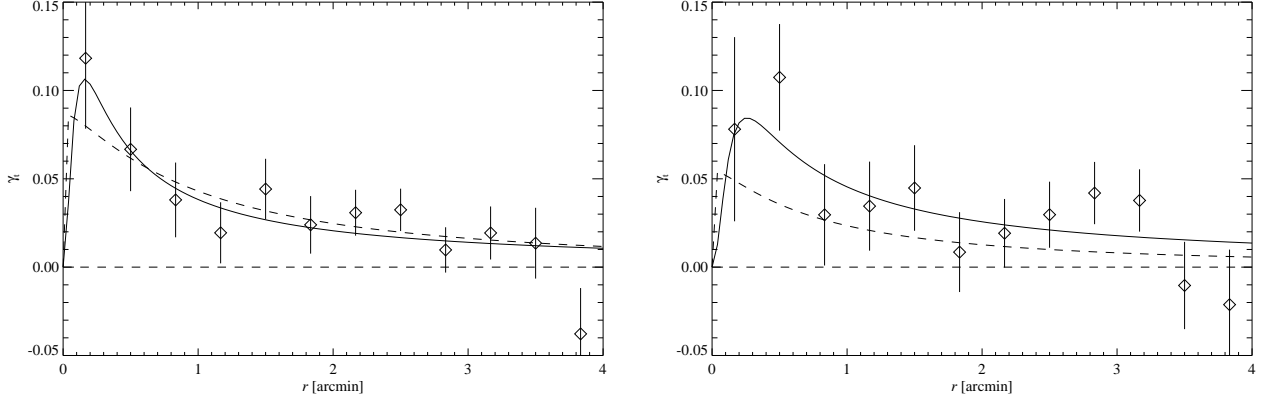


Fig. 21.— The azimuthally-averaged shear measurements on the  $i$  (left) and  $z$  (right) bands and relative errors, with overlapped the best-fit NIS (solid line) and NFW (dashed line) profiles. Note that, since individual points in this plot are independent, the detection obtained has a high statistical significance.

apparent offset toward the East of the center of the weak lensing mass.

In conclusion, the lensing mass of high-redshift clusters is likely biased toward large values because of intervening galaxy groups at lower redshifts. With accurate photometric redshifts based on our multi-wavelength observations, we will attempt to disentangle the weak lensing effects of the cluster from the ones of the main intervening masses, a method known as “weak lensing tomography” (see Taylor 2001; this analysis will be the subject of a future paper). Furthermore, strong lensing features observed around RDCS1252, which are currently under spectroscopic study, will provide further constraints on the cluster mass (see Bradac et al. 2004). The latter is expected to be much less sensitive to foreground projected masses because of the large redshifts expected for the arcs.

#### 4.4. Shear profile

It is also interesting to investigate the azimuthally averaged shear profiles, shown in Fig. 21 for both bands. We obtained this plot by computing the average tangential shear on annuli of increasing radii centered at the peak of the weak lensing mass map. The errors reported in this figure were computed from the estimated errors on the ellipticity of each galaxy. Since we used different galaxies in different bins, the various points shown are independent, which further confirms the high significance of the weak lensing detection obtained here. Overplotted is also the tangential shear prediction from the best-fit NISwl

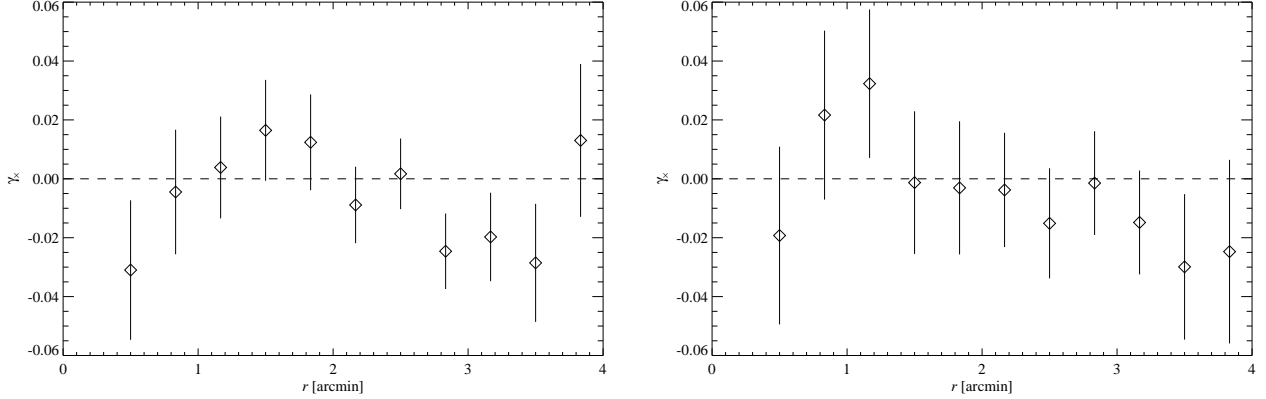


Fig. 22.— The azimuthally-averaged shear measurements transformed according to (4) on the  $i$  (left) and  $z$  (right) bands and relative errors. Since lensing is curl-free, we measurements are expected to be consistent with zero (cf. Fig. 11).

and NFWwl models.

We also evaluated the azimuthally averaged cross shear, obtained by using the transformation (4) on the galaxy ellipticities (see Fig. 22). The null detection obtained in this case is in agreement with our expectations and shows that there are no significant systematic errors in our results.

Finally, Fig. 23 shows the radial profiles obtained by azimuthally averaging the weak lensing mass maps around their peaks in the  $i$  and  $z$  band images. Despite the fact that the galaxies from which the shear is derived are the same, these two measurements are not completely dependent because of the contribution of to photometric noise to the shear error (see discussion at the end of Sect. 3.2).

## 5. Conclusion

In this paper we have discussed the weak lensing analysis of the massive cluster RDCS 1252.9–2927 at redshift  $z = 1.237$ , from deep HST/ACS observations. The combination of the excellent angular resolution and sensitivity of ACS, and an accurate measurement of the ellipticities of background galaxies have allowed us to detect a clear weak lensing signal in both the  $i$  and  $z$  SDSS bands. This result pushes weak lensing mass reconstructions to unprecedented redshifts and opens the way to new applications of this technique on the most distant clusters known to date.

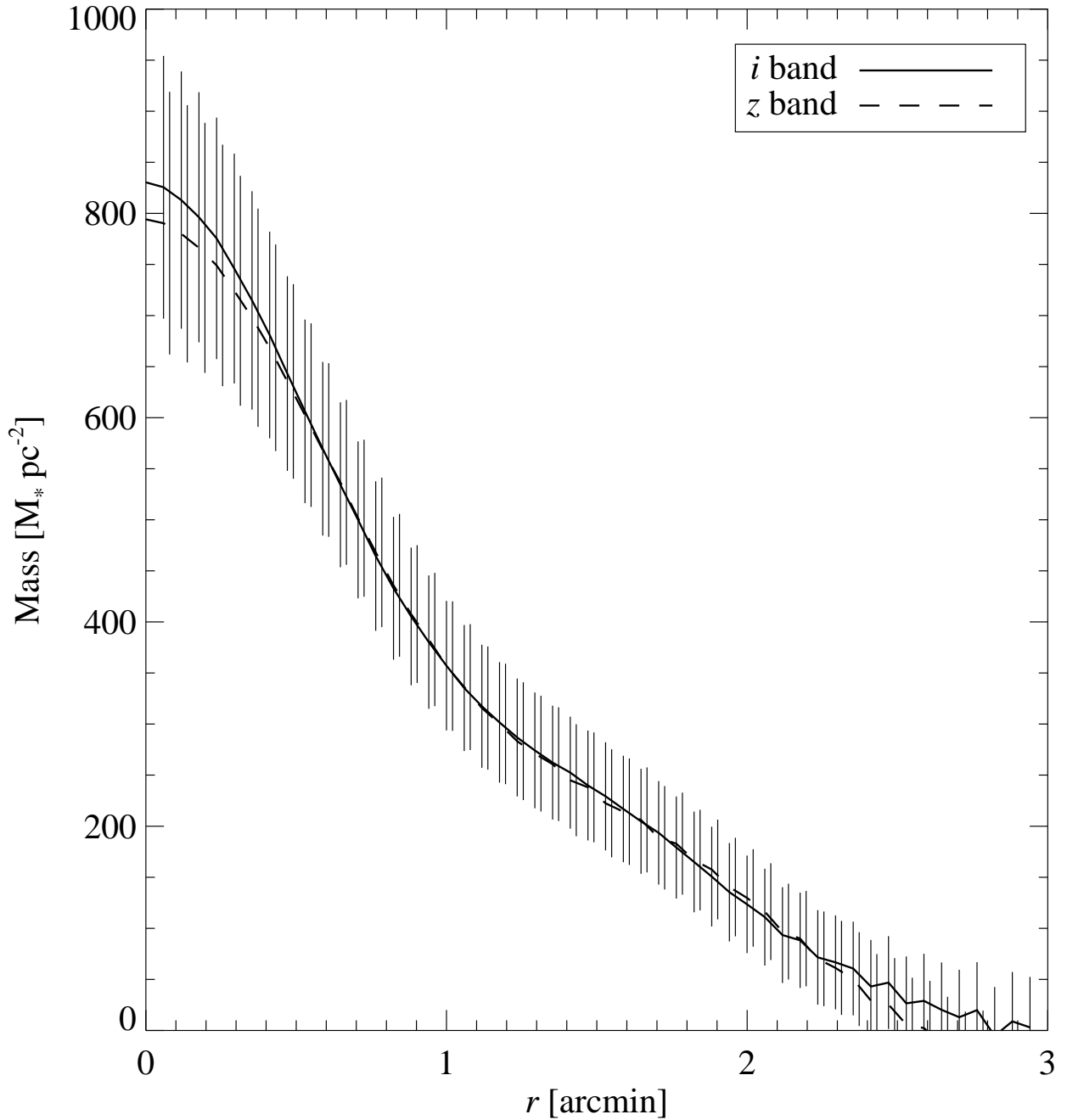


Fig. 23.— The radial mass profiles obtained from the smoothed weak lensing mass maps in the  $i$  and  $z$  band images (Fig. 6).

The main results can be summarized as follows:

- We have detected a  $5\sigma$  weak lensing signal in the  $i$  band and a  $3\sigma$  signal in the  $z$  band; the combination of the two shear maps has lead to a  $6\sigma$  detection.
- Several tests based on Monte-Carlo simulations and analytical estimates have been performed to ensure that the resulting signal is due to lensing and not to systematic effects.
- The estimate of the differential radial mass profiles in both bands has been found to be in excellent agreement with each other.
- We have fitted the observed galaxy ellipticities with simple parametric mass models (NIS and NFW) and have shown that the resulting radial profiles are statistically consistent with those obtained from the X-ray analysis.
- The spatial distribution of the dark matter, as inferred from the weak lensing map, and the one of the baryons, as traced by the X-ray emitting gas and the cluster galaxies, have a similar East-West elongation. However, we have detect an offset ( $\sim 8$  arcsec) between the centroid of the weak lensing mass map and the optical/X-ray centroid.
- We have discussed the possible sources of errors and biases of the X-ray and lensing mass estimates. We have argued that foreground galaxy groups aligned along the line of sight can alter the measured shear, thus biasing the cluster mass high, at a level which might be detected with deep ACS observations. The same argument could explain the observed offset between the weak lensing map and the optical/X-ray centroid. We have also discussed how departures from hydrostatic equilibrium and isothermality can bias the X-ray mass measurements toward larger values.

We would like to thank and Giuseppe Bertin, Tim Schrabback, Peter Schneider for stimulating discussions and useful suggestions. ACS was developed under NASA contract NAS 5-32865, and this research is supported by NASA grant NAG5-7697. We also acknowledge support from NAG5-10176. We are grateful for an equipment grant from the Sun Microsystems, Inc.

### A. Mass aperture statistics

As a further test on the lensing signal, we evaluated the mass aperture statistics (Schneider 1996). In particular, for each point of the field we estimated the quantity

$$\hat{M}_{\text{ap}}(\vec{\theta}) = \frac{\sum_{n=1}^N w_n g_{tn}(\vec{\theta}) Q(|\vec{\theta} - \vec{\theta}_n|)}{\sum_{n=1}^N w_n}, \quad (\text{A1})$$

where  $w_i$  is the weight assigned to the  $n$ -th galaxy,  $g_{tn}(\vec{\theta})$  is its shear estimate projected tangentially with respect to the point  $\vec{\theta}$ , and  $Q$  is given by

$$Q(\theta) = \frac{6}{\pi} \frac{\theta^2}{\theta_0^2} \left(1 - \frac{\theta^2}{\theta_0^2}\right). \quad (\text{A2})$$

As shown by Schneider (1996), the quantity  $\hat{M}_{\text{ap}}$  defined in Eq. (A1) is an estimate of

$$M_{\text{ap}}(\vec{\theta}) = \int d^2\theta' U(|\vec{\theta} - \vec{\theta}'|) \kappa(\vec{\theta}'). \quad (\text{A3})$$

In other words,  $\hat{M}_{\text{ap}}$  estimates the convolution of the lens convergence with a compensated filter  $U(\theta)$ . With our choice for  $Q$ , we have

$$U(\theta) = \frac{9}{\pi\theta_0^2} \left(1 - \frac{\theta^2}{\theta_0^2}\right) \left(\frac{1}{3} - \frac{\theta^2}{\theta_0^2}\right). \quad (\text{A4})$$

The quantity  $\theta_0$  sets the filter scale and, in our case, was chosen to be  $\theta_0 = 2'30''$ . This particular choice for  $\theta_0$  maximizes the signal-to-noise ratio and can be justified by observing that, at the cluster redshift, this scale is 1.3 Mpc, i.e. approximately the cluster size.

We evaluated the mass aperture  $M_{\text{ap}}$  for both the  $i$  and  $z$ -band catalogs using a filter scale  $\theta_0/5 = 30$  arcsec. In both bands we observed a prominent peak at the position of the cluster. Because of the simple functional form of  $M_{\text{ap}}$ , it is straightforward to evaluate the expected noise on this quantity and thus to infer the significance of the detection obtained. Thus, we were able to confirm the  $5\sigma$  significance in  $i$  and the  $3\sigma$  in  $z$  bands.

## REFERENCES

- Bahcall, N. A. & Fan, X. 1998, ApJ, 504, 1  
 Bartelmann, M. 1996, A&A, 313, 697  
 Bartelmann, M. & Schneider, P. 2001, Physics Reports, 340, 291

- Benitez, N. 2000, *ApJ*, 536, 571
- Blakeslee, J. P., Anderson, K. R., Meurer, G. R., Benítez, N., & Magee, D. 2003a, in ASP Conf. Ser. 295: Astronomical Data Analysis Software and Systems XII, 257
- Blakeslee, J. P., Franx, M., Postman, M., Rosati, P., Holden, B. P., Illingworth, G. D., Ford, H. C., Cross, N. J. G., Gronwall, C., Benítez, N., Bouwens, R. J., Broadhurst, T. J., Clampin, M., Demarco, R., Golimowski, D. A., Hartig, G. F., Infante, L., Martel, A. R., Miley, G. K., Menanteau, F., Meurer, G. R., Sirianni, M., & White, R. L. 2003b, *ApJ*, 596, L143
- Bradac, M., Schneider, P., Lombardi, M., & Erben, T. 2004, ArXiv Astrophysics e-prints
- Cavaliere, A. & Fusco-Femiano, R. 1976, *A&A*, 49, 137
- . 1978, *A&A*, 70, 677
- Clowe, D., De Lucia, G., & King, L. 2004, *MNRAS*, 350, 1038
- Clowe, D., Luppino, G., Kaiser, N., Henry, J., & Gioia, I. 1998, *ApJ*, 497, L61
- Eadie, W., Drijard, D., James, F., Roos, M., & Sadoulet, B. 1971, Statistical Methods in Experimental Physics (Amsterdam New-York Oxford: North-Holland Publishing Company)
- Efron, B. 1982, The Jackknife, the Bootstrap and other resampling plans (Bristol, England: Society for Industrial and Applied Mathematics)
- Eke, V. R., Cole, S., & Frenk, C. S. 1996, *MNRAS*, 282, 263
- Erben, T., Van Waerbeke, L., Bertin, E., Mellier, Y., & Schneider, P. 2001, *A&A*, 366, 717
- Ettori, S., Tozzi, P., Borgani, S., & Rosati, P. 2004, *A&A*, 417, 13
- Fernández-Soto, A., Lanzetta, K. M., & Yahil, A. 1999, *ApJ*, 513, 34
- Fruchter, A. S. & Hook, R. N. 2002, *PASP*, 114, 144
- Gal, R. R. & Lubin, L. M. 2004, *ApJ*, 607, L1
- Hoekstra, H., Franx, M., & Kuijken, K. 2000, *ApJ*, 532, 88
- Huo, Z., Xue, S., Xu, H., Squires, G., & Rosati, P. 2004, *AJ*, 127, 1263
- Kaiser, N., Squires, G., & Broadhurst, T. 1995, *ApJ*, 449, 460

- King, L. J., Clowe, D. I., & Schneider, P. 2002, A&A, 383, 118
- Lanzetta, K. M., Yahata, N., Pascarelle, S., Chen, H., & Fernández-Soto, A. 2002, ApJ, 570, 492
- Lidman, C., Rosati, P., Demarco, R., Nonino, M., Mainieri, V., Stanford, S. A., & Toft, S. 2004, A&A, 416, 829
- Lombardi, M. & Bertin, G. 1998, A&A, 335, 1
- . 1999a, A&A, 348, 38
- . 1999b, A&A, 342, 337
- Lombardi, M., Rosati, P., Nonino, M., Girardi, M., Borgani, S., & Squires, G. 2000, A&A, 363, 401
- Luppino, G. A. & Kaiser, N. 1997, ApJ, 475, 20
- Margoniner, V. E., Lubin, L. M., Wittman, D. M., & Squires, G. K. 2005, AJ, 129, 20
- Marshall, P. J., Hobson, M. P., Gull, S. F., & Bridle, S. L. 2002, MNRAS, 335, 1037
- Metzler, C. A., White, M., & Loken, C. 2001, ApJ, 547, 560
- Postman, M., Lubin, L. M., & Oke, J. B. 1998, AJ, 116, 560
- Rosati, P., della Ceca, R., Norman, C., & Giacconi, R. 1998, ApJ, 492, L21+
- Rosati, P., Tozzi, P., Ettori, S., Mainieri, V., Demarco, R., Stanford, S. A., Lidman, C., Nonino, M., Borgani, S., Della Ceca, R., Eisenhardt, P., Holden, B. P., & Norman, C. 2004, AJ, 127, 230
- Schlegel, D. J., Finkbeiner, D. P., & Davis, M. 1998, ApJ, 500, 525
- Schneider, P. 1996, MNRAS, 283, 837
- Seitz, C., Kneib, J.-P., Schneider, P., & Seitz, S. 1996, A&A, 314, 707
- Seitz, C. & Schneider, P. 1997, A&A, 318, 687
- Seitz, S. & Schneider, P. 1996, A&A, 305, 383
- Smail, I., Ellis, R. S., & Fitchett, M. J. 1994, MNRAS, 270, 245
- Squires, G., Kaiser, N., Fahlman, G., Babul, A., & Woods, D. 1996, ApJ, 469, 73

Taylor, A. N. 2001, ArXiv Astrophysics e-prints

Toft, S., Mainieri, V., Rosati, P., Lidman, C., Demarco, R., Nonino, M., & Stanford, S. A. 2004, ArXiv Astrophysics e-prints

Tyson, J., Wenk, R., & Valdes, F. 1990, ApJ, 349, L1

White, M., van Waerbeke, L., & Mackey, J. 2002, ApJ, 575, 640